JOURNAL OF GEOPHYSICAL RESEARCH, VOL. ???, XXXX, DOI:10.1002/,

Turbulent boundary layers under irregular waves and currents: experiments and the equivalent-wave concept

Jing Yuan,[1]

[1]Department of Civil and Environmental Engineering, National University of Singapore, Singapore

Key Points.

- A full-scale experimental study of boundary layer flows under irregular waves and currents.
- PIV measurement of boundary layer flows.
- Irregular waves can be represented by an equivalent periodic wave.

Abstract. A full-scale experimental study of turbulent boundary layer flows under irregular waves and currents is conducted with the primary objective to investigate the equivalent-wave concept by *Madsen* [1994]. Irregular oscillatory flows following the bottom-velocity spectrum under realistic surface irregular waves are produced over two fixed rough bottoms in an oscillatory water tunnel, and flow velocities are measured using a Particle Image Velocimetry. The root-mean-square (RMS) value and representative phase lead of wave velocities have vertical variations very similar to those of the first-harmonic velocity of periodic wave boundary layers, e.g. the RMS wave velocity follows a logarithmic distribution controlled by the physical bottom roughness in the very near-bottom region. The RMS wave bottom shear stress and the associated representative phase lead can be accurately predicted using the equivalent-wave approach. The spectra of wave bottom shear stress and boundary layer velocity are found to be proportional to the spectrum of free-stream velocity. Currents in the presence of irregular waves exhibit the classic two-log-profile structure with the lower log-profile controlled by the physical bottom roughness and the upper log-profile controlled by a much larger apparent roughness. Replacing the irregular waves by their equivalent sinusoidal waves virtually makes no difference for the co-existing cur-

rents. These observations, together with the excellent agreement between measurements and model predictions, suggest that the equivalent-wave representation adequately characterizes the basic wave-current interaction under irregular waves.

1. Introduction

In the coastal environment co-existing waves and currents nonlinearly interact with each other near the seabed under turbulent flow conditions, leading to a turbulent wave-current boundary layer (WCBL). A good understanding of WCBL is the prerequisite for modeling coastal sediment transport, as it directly determines bottom shear stress for bedload transport and near-bottom flow velocity carrying suspended-load transport. Therefore, WCBL has been extensively studied in the past decades.

Wave boundary layers, even under extreme wave conditions, are usually very thin (a few centimeters) due to the limited time scale (a wave period) for boundary layer development, while current boundary layers can extend over the entire water depth (several meters). Thus, a WCBL is controlled by turbulence produced by both waves and currents within the wave boundary layer, but only current-produced turbulence outside the wave boundary layer. Following this concept, the widely-used *Grant and Madsen* [1979] model (GM model hereafter) adopts a bi-linear time-invariant turbulent eddy viscosity for modeling the Reynolds stress in the linearized horizontal momentum equation, i.e. the turbulent eddy viscosity is scaled with the combined maximum shear velocity within the wave boundary layer, but is scaled with the current shear velocity outside the wave boundary layer. Their analytical solution of the current velocity profile suggests that currents are significantly retarded by co-existing waves, which can be conceptualized by a large apparent roughness experienced by currents. This mechanism is supported by many field [e.g. *Drake and Cacchione*, 1992] and laboratory [e.g. *Mathisen and Madsen*, 1996a, b] observations, and we hereafter identify it as the basic wave-current interaction.

Waves can also modify currents by producing boundary layer streamings through two mechanisms. The boundary layer flow under progressive surface waves will have certain spatial inhomogeneity in the wave direction, which leads to a small vertical velocity within the bottom boundary layer. The vertical and horizontal velocities are not completely 90° out of phase, so the convective terms in the horizontal momentum equation have non-zero period-averaged values, leading to a mean current (progressive wave streaming). *Longuet-Higgins* [1953] first analytically explained this phenomenon for laminar flows and later extended his analysis for turbulent flows in the appendix to *Russell and Osorio* [1958]. He showed that the progressive wave streaming is always in the wave direction. Another mechanism for wave boundary layer streaming is associated with wave nonlinearities (hereafter referred to as turbulence asymmetry streaming). The bottom wave orbital velocity under nonlinear surface waves exhibits some asymmetric features between successive half-periods [e.g. *Berni et al.*, 2013], which is often characterized by velocity-skewness and acceleration-skewness. Thus, the temporal variation of turbulence characteristics within the two half-periods are not symmetric, which can be modeled with a time-varying turbulent eddy viscosity. Following this concept, *Trowbridge and Madsen* [1984a, b] analytically showed that a boundary layer streaming in the opposite direction of wave propagation can be produced by turbulence asymmetry, which was first observed in the oscillatory-water-tunnel experiments by *Ribberink and Al-Salem* [1995]. In recent years, numerical models has been applied to study the co-existence of the two kinds of wave boundary layer streaming [e.g. *Holmedal and Myrhaug*, 2009; *Kranenburg et al.*, 2012; *Blondeaux et al.*, 2012]. The general conclusion is that the relative importance of one streaming over the other depends on the shallowness of the water and also bottom roughness. *Yuan* *and Madsen* [2015] (YM15 hereafter) reported experiments of currents in the presence of asymmetry oscillatory flows, and showed that the turbulence asymmetry streaming has a pronounced effect on currents, which can even invalidate the basic wave-current interaction proposed by the GM model. *Holmedal et al.* [2013] and *Afzal et al.* [2015], among others, numerically showed that the effects of both progressive and turbulent asymmetry streamings on wave-current interactions can be very significant.

Most existing studies on turbulent WCBL are based on regular (or periodic) waves, while in really we always have irregular waves in the coastal environment. Except for some numerical studies, e.g. *Holmedal et al.* [2003] and *Tanaka and Samad* [2006], which can directly model the boundary layer flow under irregular waves in the time domain, the vast majority of theoretical works adopt two general approaches to describe the wave irregularity: probabilistic and spectral approaches.

For the probabilistic approach, irregular waves are treated as a package of independent periodic waves following a specified probability distribution, e.g. *Dally* [1992], *Grasmeijer and Ruessink* [2003] and *Yuan and Madsen* [2010]. Therefore, the existing models for periodic WCBL can be directly applied for individual periodic waves to obtain the probability distributions for certain variables of interest, e.g. maximum wave bottom shear stress [*Myrhaug et al.*, 2001], or some deterministic physical quantities through probabilistically averaging, e.g. current velocity [*Yuan and Madsen*, 2010]. The fundamental drawback of this approach is that some physical processes, e.g. boundary layer streaming, may not have immediate response to the change of wave conditions, so it is questionable to assume that individual waves are totally independent.

The spectral approach describes irregular waves by a directional wave energy spectrum. Among similar studies, the spectral wave-current boundary layer model developed by *Madsen* [1994] (hereafter M94) is the widely-used for analyzing field data, e.g. *Nayak et al.* [2015]. In this model, the bottom wave orbital velocity is described by a directional velocity spectrum, which can be discretized into a set of infinitesimal wave components. By modeling the Reynolds stress with the bi-linear time-invariant turbulent eddy viscosity proposed by *Grant and Madsen* [1979], the boundary layer equations for each wave component and the current are completely linear and can be analytically solved. The most important finding is that a representative sinusoidal wave can be used to represent the irregular waves in modeling basic wave-current interaction. Therefore, the GM model for periodic WCBL is easily extended to irregular-wave scenarios. *Holmedal et al.* [2003] "indirectly" validated the concept of equivalent wave through numerical experiments, but so far there is no "direct" validations possibly due to the lack of suitable measurements.

Very few detailed laboratory investigations on irregular WCBL are reported in public literatures. *Mathisen and Madsen* [1999] conducted experiments of irregular waves with or without collinear currents over a fixed rippled bed in a small-scale wave flume. Their measurements of current velocity profiles suggest that the basic wave-current interaction indeed can be predicted with the equivalent-wave approach proposed by M94 with some minor modifications, and a single bottom roughness controls waves (periodic or irregular) and currents over a fixed rough bottom configuration. However, their experiments are with very large bottom roughness to ensure turbulent flow conditions, which is outside the M94's range of applicability. *Klopman* [1994] reported an wave-flume study similar to *Mathisen and Madsen* [1996a, b, 1999] but with smaller fixed bottom roughness elements.

Their results showed that random waves significantly retard the currents within the wave boundary layer. *Simons et al.* [1994] reported shear-plate measurement of bottom shear stresses under irregular waves with or without currents in a wave basin. A common problem among most experimental studies is that they do not correspond to full-scale flow conditions. A wave boundary layer, which can induce noticeable amounts of sediment transport, usually has a near-bottom wave orbital velocity amplitude U_b of the order 1 m/s, or a Reynolds number $Re = A_b U_b/\nu$ up to $O(10^5 \sim 10^6)$, where A_b is the excursion amplitude and ν is the water kinematic viscosity. Small-scale laboratory wave flumes or wave basins can only achieve a Reynolds number of $O(10^3 \sim 10^4)$. Therefore, another type of facility, Oscillatory Water Tunnel (OWT), is designed for full-scale simulation of boundary layer flows under surface waves. These facilities are essentially U-shaped tunnels with a piston driving oscillatory flows over the entire facility, so very high Reynolds number can be easily achieved. For some OWTs, a current circulation system can superimpose a collinear current on the oscillatory flows to produce WCBL flows. The major disadvantage of OWTs is that the generated oscillatory flows are approximations of the actual wave boundary layers due to the absence of vertical velocity component, so certain physics are excluded, e.g. progressive wave streaming. Nevertheless, OWT experiments still have high research values, as the dominant physics are still captured. To the author's knowledge, no OWT experiment with detailed flow measurements of irregular WCBLs has been reported in public literatures.

This paper presents a full-scale OWT experimental study of turbulent boundary layer flows under irregular waves and currents over rough bottoms with well-known bottom roughness. The primary objective is to validate whether the basic wave-current interaction under irregular waves follows the equivalent-wave concept proposed by M94. The paper begins with a brief review of the M94 model, which is taken as the theoretical foundation for this study, in section 2. The experimental conditions are presented in section 3. Section 4 presents experimental results on wave velocities and wave bottom shear stress, and section 5 discusses the measurements on current velocity profiles. Conclusions and some discussions are given in section 6.

2. Madsen (1994) model for spectral wave-current boundary layer

Since the currents and oscillatory flows in this study are always collinear due to the limitation of facility, the collinear version of the M94 model is briefly reviewed here for later reference, and the reader is referred to M94 for waves and currents at an angle. The governing equation for this model is the linearized boundary layer equation:

$$\frac{\partial u}{\partial t} = -\frac{\partial}{\partial x}\left(\frac{p}{\rho}\right) + \frac{\partial}{\partial z}\left(\nu_T \frac{\partial u}{\partial z}\right) \tag{1}$$

where u is horizontal velocity, t is time, p is pressure, ρ is water density, (x, z) are horizontal and vertical coordinates, and ν_T is the turbulent eddy viscosity. Following the argument for basic wave-current interaction, a time-invariant ν_T is proposed with the following bi-linear vertical structure:

$$\nu_T = \begin{cases} \kappa u_{*cw} z, \, z < \delta_{cw} \\ \kappa u_{*c} z, \, z \geq \delta_{cw} \end{cases} \tag{2}$$

where κ is the von Karman constant, δ_{cw} is the transition level, $u_{*c} = \sqrt{\tau_{cb}/\rho}$ is the current shear velocity with τ_{cb} being the current bottom shear stress, and u_{*cw} is an a priori unknown wave-current shear velocity which reflects the combined wave-current flow inside the wave boundary layer. Separating velocity and pressure into their mean and time-varying components, i.e.: $u = u_c + u_w$ and $p = p_c + p_w$, where the subscripts "c" and "w" denote current and wave, respectively. Equation (1) can be separated into a wave equation:

$$\frac{\partial u_w}{\partial t} = \frac{\partial u_\infty}{\partial t} + \frac{\partial}{\partial z}\left(\nu_T \frac{\partial u_w}{\partial z}\right) \tag{3}$$

and a current equation:

$$\nu_T \frac{\partial u_c}{\partial z} = \frac{\tau_{cb}}{\rho} = {u_{*c}}^2 \tag{4}$$

in which the law-of-the-wall arguments have been used. The free-stream wave velocity $u_\infty(t)$ associated with a velocity spectrum $S_{Ub}(\omega)$ can be expressed as:

$$u_\infty(t) = \mathrm{Re}\left[\sum_n u_{\infty,n} e^{i\omega_n t}\right] \tag{5}$$

where n denotes summation over frequencies and the amplitude of a wave component $|u_{\infty,n}|$ with radian frequency ω_n is given by $|u_{\infty,n}| = \sqrt{2S_{Ub}(\omega_n)d\omega}$. The linearity of Equation (3) and a time-invariant ν_T suggest the follow solutions of velocity and bottom shear stress:

$$u(z,t) = \mathrm{Re}\left[\sum_n u_n(z) e^{i\omega_n t}\right] \tag{6}$$

and:

$$\tau_b(t) = \mathrm{Re}\left[\sum_n \tau_{bn} e^{i\omega_n t}\right] \tag{7}$$

respectively. With the no-slip boundary condition specified at

$$z = z_0 = k_b/30 \tag{8}$$

where k_b is bottom roughness, analytical solutions for $u_n(z)$ can be expressed as:

$$u_n(z) = F(\omega_n, z) u_{\infty,n} = \left[1 - \frac{\ker 2\sqrt{z\omega_n/\kappa u_{*cw}} + i\mathrm{kei}2\sqrt{z\omega_n/\kappa u_{*cw}}}{\ker 2\sqrt{z_0\omega_n/\kappa u_{*cw}} + i\mathrm{kei}2\sqrt{z_0\omega_n/\kappa u_{*cw}}}\right] u_{\infty,n} \tag{9}$$

where ker and kei are Kelvin functions of order zero, see *Abramowitz and Stegun* [1965]. Bottom shear stress τ_{bn} is evaluated at $z = z_0$ with the obtained $u_n(z)$, and the result can be expressed as:

$$\tau_{bn} = K(\omega_n)u_{\infty,n} = \rho\kappa u_{*cw}\sqrt{\frac{z_0\omega_n}{\kappa u_{*cw}}}\left[\frac{-\ker' 2\sqrt{\frac{z_0\omega_n}{\kappa u_{*cw}}} - i\text{kei}' 2\sqrt{\frac{z_0\omega_n}{\kappa u_{*cw}}}}{\ker 2\sqrt{\frac{z_0\omega_n}{\kappa u_{*cw}}} + i\text{kei} 2\sqrt{\frac{z_0\omega_n}{\kappa u_{*cw}}}}\right] u_{\infty,n} \tag{10}$$

in which "prime" denotes the derivative of the zeroth order Kelvin functions with respect to its argument. Both $F(\omega_n, z)$ and $K(\omega_n)$ are weak functions of ω for small bottom roughness [*Madsen et al.*, 1988], so the spectra $S_U(\omega, z)$ and $S_{\tau b}(\omega)$ can be approximated as:

$$S_U(\omega, z) \approx |F^2(\omega_{ave}, z)| S_{Ub}(\omega) \tag{11}$$

and

$$S_{\tau b}(\omega) \approx |K^2(\omega_{ave})| S_{Ub}(\omega) \tag{12}$$

respectively, where the average radian frequency ω_{ave} associated with the average wave period T_{ave} is defined as:

$$\omega_{ave} = \frac{2\pi}{T_{ave}} = \frac{\int \omega S_{Ub}(\omega) d\omega}{\int S_{Ub}(\omega) d\omega} \tag{13}$$

Thus, both $S_U(\omega, z)$ and $S_{\tau b}(\omega)$ are approximately proportional to $S_{Ub}(\omega)$, suggesting that the Root-mean-square (RMS) wave velocity $U_{rms}(z)$ and RMS wave bottom shear stress $\tau_{b,rms}$ can be simply related to the RMS free-stream velocity $U_{\infty,rms}$ through:

$$U_{rms}(z) \approx |F(\omega_{ave}, z)| U_{\infty,rms} \tag{14}$$

and

$$\tau_{b,rms} \approx |K(\omega_{ave})| U_{\infty,rms} \tag{15}$$

respectively. A two-log-profile structure for current velocity profile is obtained by solving Equation (4):

$$u_c = \begin{cases} \dfrac{u_{*c,1}}{\kappa}\ln\left(\dfrac{z}{z_0}\right) = \dfrac{u_{*c}^2}{\kappa u_{*cw}}\ln\left(\dfrac{z}{z_0}\right), & z < \delta_{cw} \\ \dfrac{u_{*c,2}}{\kappa}\ln\left(\dfrac{z}{z_{0a}}\right) = \dfrac{u_{*c}}{\kappa}\ln\left(\dfrac{z}{z_{0a}}\right), & z \geqslant \delta_{cw} \end{cases} \tag{16}$$

where $z_{0a} = k_{Na}/30$ with k_{Na} being the apparent roughness is obtained by matching the two log-profiles at the transition level δ_{cw}. Therefore, z_{0a} is closely related to δ_{cw}. M94 simply took $\delta_{cw}/l = 2$, where:

$$l = \frac{\kappa u_{*cw}}{\omega_{ave}} \tag{17}$$

is a characteristic wave boundary layer scale. The closure for u_{*cw} is achieved by requiring the spectral wave-current model to reduce to the Grant-Madsen model, i.e. u_{*cw} becomes the maximum shear velocity based on the maximum bottom shear stress, in the limit of simple periodic waves. For collinear waves and currents, u_{*cw} is given by:

$$u_{*cw} = \sqrt{{u_{*c}}^2 + {u_{*w}}^2} \tag{18}$$

where the wave shear velocity u_{*w} is defined as:

$$u_{*w} = \begin{cases} \sqrt{\tau_{b,rms}/\rho}, & \text{irregular wave} \\ \sqrt{\tau_{wm}/\rho}, & \text{periodic wave} \end{cases} \tag{19}$$

with τ_{wm} being the maximum wave bottom shear stress for periodic waves. Based on Equations (11), (12), (16) and (18), it can be easily seen that the if irregular waves are represented by a sinusoidal wave with $U_{\infty,rms}$ as velocity amplitude and T_{ave} as wave period, the same effect of waves on currents can be obtained, and $U_{rms}(z)$ and $\tau_{b,rms}$ are just the velocity amplitude and maximum wave bottom shear stress of the equivalent sinusoidal wave, respectively. Thus, the periodic-wave-based GM model can be easily extended to irregular-wave scenarios.

The predicative ability of the original GM model is not always satisfactory due to some oversimplifications, e.g. the transition level δ_{cw} for the discontinuous bi-linear turbulent eddy viscosity ν_T is rather arbitrarily-define, so it has been improved for a few times. *Humbyrd* [2012] provided the latest and most consistent improvement of the GM model (hereafter the improved GM model). This model adopts a three-layer continuous structure for ν_T with rigorously defined transition levels (see appendix A for details). The analytical solution of the current velocity profile is two log-profiles connected by a smooth transition. Translating this more realistic current profile into the simpler two-log-profile structure defined by Equation (16), the normalized transition level δ_{cw}/l is analytically obtained, and is shown to be a function of $\alpha = u_{*c}/u_{*cw}$. The maximum wave bottom shear stress τ_{wm} predicted by the improved GM model is translated into a wave friction factor $f_{cw} = 2\tau_{wm}/(\rho {U_b}^2)$. Explicit formulas for f_{cw} under wave-current conditions are obtained from fitting analytical solutions. For the applicable range of our tests the formula can be simplified as:

$$\frac{f_{cw}}{C_\mu} = \exp\left\{5.70\left(C_\mu \frac{A_b}{k_b}\right)^{-0.101} - 7.46\right\}, \quad 10 < C_\mu \frac{A_b}{k_b} < 10^5 \tag{20}$$

where C_μ is a parameter representing the effect of currents:

$$C_\mu = (1-\alpha^2)^{-1} \tag{21}$$

For pure wave boundary layers the wave friction factor is obtained by taking $C_\mu = 1$. The maximum wave bottom shear stress leads the maximum free-stream velocity in phase. Explicit formula for the phase lead φ_τ is also obtained from fitting analytical solutions, and for the applicable range of our tests φ_τ can be approximately given by:

$$\varphi_\tau = \left[0.649\left(C_\mu \frac{A_b}{k_b}\right)^{-0.160} + 0.118\right]\frac{180}{\pi}[^\circ], \quad 10 < C_\mu \frac{A_b}{k_b} < 10^5 \tag{22}$$

In this study, the improved GM model is used for applying the equivalent-wave concept proposed by M94, and this combination is hereafter referred to as the improved M94 model.

3. Experimental conditions

3.1. Experimental facility

The tests in this study are conducted using the Wave-Current-Sediment (WCS) facility at the hydraulic lab of the Civil and Environmental Engineering Department of National University of Singapore. The WCS is essentially a U-shaped oscillatory water tunnel. The main part is a 10m-long, 40cm-wide and 50cm-deep enclosed horizontal test channel with two cylindrical risers attached to the channel's two ends. A hydraulic-driven piston located in one of the risers produces oscillatory flows over the entire facility with flow velocities and accelerations up to 2 m/s and 2 m/s^2, respectively, so full-scale flow conditions, i.e. $Re \sim O(10^5 \sim 10^6)$, can be easily achieved. A current generation system driven by a rotary-lobe pump can superimpose currents with a cross-section average velocity up to 60 cm/s on oscillatory flows. Previous studies by *Yuan and Madsen* [2014] (YM14 hereafter) and YM15 suggest that the facility can precisely produce intended oscillatory flows and currents, and the reader is referred to these two publications for more details on flow generation and other details about the WCS.

A 2D Particle Image Velocimeter (PIV) system supplied by TSI Corporation is used for measuring boundary layer flows in the vertical plane of the lateral centerline of the test channel. The measurement site is located around the longitudinal center of the test channel to minimize end effects. For all tests in this study, the vertical resolution is about 0.6 mm/grid, which gives a roughly 12 cm-by-12 cm observation window. This is close to the highest resolution that the PIV can offer with the present experimental setup, and is sufficient for revealing key Reynolds-averaged characteristics of boundary layer flows in this study. Due to laser reflection on the bottom, the lowest level with valid PIV measurement is about $1 \sim 2$ mm above the crests of roughness elements. The reader is referred to YM14 for more details on the PIV system. Since the flow in the WCS is longitudinally uniform, the velocities measured at the same vertical level effectively have the same Reynolds average velocity, so the 2D velocity field measured by the PIV can be horizontally averaged into a Reynolds-averaged velocity profile:

$$< \xi(z,t) >= \frac{1}{I}\sum_{i=1}^{I} \xi(x_i, z, t) \tag{23}$$

where ξ is either the horizontal or vertical component of flow velocity (u, w) and x_i is the horizontal coordinate of the i-th velocity measurement of the total I velocity measurements at level z. Unless otherwise indicated, $\xi(z,t)$ will denote the Reynolds-averaged quantities throughout the remainder of this paper. It has been shown by YM14 that the measurements of turbulence statistics in the WCS, e.g. Reynolds stress, is not quantitatively reliable due to the averaging nature of PIV. Meanwhile, the focus of this paper is irregular-wave-current interaction in terms of the Reynolds-averaged flow, so no measurements about turbulence will be discussed in this paper.

3.2. Bottom conditions

As suggested by Equations (20) and (22), wave boundary layer flows are controlled by the relative bottom roughness A_b/k_b. To cover a wide range of A_b/k_b, two fixed rough bottoms are used in this study. One is created by gluing 3MTM 710 Safety-Walk(TM) Slip-Resistant Coarse tapes (physical roughness height of about 1 mm) onto smooth aluminum plates, and is hereafter referred to as the sandpaper bottom. The other consists of a mono-layer of 12.5 mm-diameter ceramic marbles glued onto aluminum plates, and is hereafter referred to as the ceramic-marble bottom. YM14 conducted careful log-profile fitting analysis for several pure current and pure sinusoidal wave tests to quantify the theoretical bottom location $z = 0$ and equivalent Nikuradse sand grain roughness k_N for these two bottoms. For the sandpaper bottom, $z = 0$ is found to be 0.6 ± 0.1 mm below the mean crest level of bottom roughness elements and k_N is 3.7 ± 0.1 mm. For the ceramic-marble bottom, $z = 0$ is 4.0 ± 0.4 mm (roughly 1/3 of the ceramic marbles' diameter) below the top of the marbles and k_N is 20 ± 3 mm.

3.3. Flow conditions

To produce oscillatory flows in the WCS, which can realistically simulate the bottom wave velocity under irregular waves, we start with considering conceptual surface waves characterized by a Joint North Sea Wave Project (JONSWAP) spectrum [*Hasselmann et al.*, 1973] modified for finite depth. The spectral density of a JONSWAP spectrum is given by:

$$S_J(\omega) = \frac{\alpha g^2}{\omega^5} \exp\left[-\frac{5}{4}\left(\frac{\omega}{\omega_p}\right)^{-4}\right] \gamma^{\exp\left[\frac{-(\omega/\omega_p - 1)^2}{2\sigma^2}\right]} \tag{24}$$

where α is Philip's constant, $\gamma = 3.3$ is a peak enhancement factor, g is gravitational acceleration, ω_p is the radian frequency associated with the peak spectral density and σ is a spectral width factor given by:

$$\sigma = \begin{cases} 0.07, & \text{if} \quad \omega \leq \omega_p \\ 0.09, & \text{if} \quad \omega > \omega_p \end{cases} \tag{25}$$

In finite water depth, *Graber* [1984] following *Kitaigordskii et al.* [1975] derived a finite-depth JONSWAP spectrum, which can be expressed as:

$$S_{\eta\eta} = \phi(\omega) S_J \tag{26}$$

where:

$$\phi(\omega) = \chi^{-2}\left[1 + \omega^2 \frac{h}{g}(\chi^2 - 1)\right]^{-1} \tag{27}$$

in which h is water depth and χ is obtained from:

$$\chi \tanh(\frac{h\omega^2}{g}\chi) = 1 \tag{28}$$

Using linear wave theory, the spectrum of near-bottom wave orbital velocity is:

$$S_{Ub}(\omega) = \frac{\omega^2 S_{\eta\eta}(\omega)}{\sinh^2(kh)} \tag{29}$$

where k is the wave number obtained from the linear dispersion relationship:

$$\omega^2 = gk\tanh(kh) \tag{30}$$

Thus, by tuning the parameters, α and ω_p, for the JONSWAP spectrum in Equation (24), a $S_{Ub}(\omega)$ with pre-determined target values for RMS wave velocity $U_{\infty,rms}$ and average radian frequency ω_{ave} (or average wave period $T_{ave} = 2\pi/\omega_{ave}$) can be obtained, which is taken as the spectrum of free-stream velocity in the WCS. A realization of free-stream velocity is obtained from a discretization of S_{Ub}:

$$u_\infty(t) = \sum_{n=1}^{N} u_{\infty,n}\cos(n\Delta\omega t + \varphi_n) = \sum_{n=1}^{N}\sqrt{2S_{Ub}(n\Delta\omega)\Delta\omega}\cos(n\Delta\omega t + \varphi_n) \tag{31}$$

where φ_n is the randomly-generated phase of the n-th wave component and $\Delta\omega$ is the discretization interval. This realization has a recurrence period of $T_{recur} = 2\pi/\Delta\omega$, so $\Delta\omega$ should be as small as possible to maximize T_{recur}. In this study T_{recur} is limited by the longest duration of a continuous PIV measurement (limited by the RAM of PIV computer), which is about 500 seconds with a sampling frequency of 5.12 Hz. Thus, $\Delta\omega$ is chosen to give a recurrence period of $T_{recur} = 500$ s to allow a continuous PIV measurement for one recurrence period. $u_\infty(t)$ is converted to the control signal for WCS piston displacement $s(t)$ based on the principle of continuity.

Two conceptual waves are considered in this study: a short-period wave (W1) with $T_{ave} = 6.25$ s and $U_{\infty,rms} = 0.85$ m/s at a water depth of $h = 12$ m and a long-period wave (W2) with $T_{ave} = 12.5$ s and $U_{\infty,rms} = 0.55$ m/s at a water depth of $h = 40$ m. The corresponding Reynolds numbers $Re = U_{\infty,rms} A_{\infty,rms}/\nu$ are close to $1.0 \cdot 10^6$, indicating full-scale flow conditions. The characteristic parameters of the spectra are shown in Table 1. A recurrence period (500 s) includes about 40 or 80 individual waves for the two wave conditions, which should be sufficient to realistically account for the wave irregularity. Since the primary objective of this study is to investigate the basic wave-current interaction under irregular waves, $u_\infty(t)$ is expected to exhibit very little nonlinear feature to exclude turbulence asymmetry streaming. Following *O'Donoghue et al.* [2006] the nonlinearity is represented by a parameter R_u characterizing the velocity-skewness:

$$R_u = \frac{u_{c,1/3}}{u_{c,1/3} - u_{t,1/3}} \tag{32}$$

where $u_{c,1/3}$ and $u_{t,1/3}$ are the averages of the highest 1/3 positive and negative maximums of $u_\infty(t)$, and another parameter R_a characterizing the acceleration-skewness:

$$R_a = \frac{a_{c,1/3}}{a_{c,1/3} - a_{t,1/3}} \tag{33}$$

where $a_{c,1/3}$ and $a_{t,1/3}$ are the highest 1/3 positive and negative maximums of $du_\infty(t)/dt$. A few realizations of $u_\infty(t)$ are generated for each wave condition with randomly-assigned phase φ_n in Equation (31), and the one with R_u and R_a closest to 0.5 (indicating little nonlinear features) is taken as the final choice. Figure 1(a,b) shows the chosen two realizations for the two wave conditions. The times series appear very "symmetric", i.e. one would not notice any difference if the time series is flipped around $u = 0$. To facilitate the comparison between the wave spectrum $S_{\eta\eta}$ and free-stream velocity spectrum S_{Ub}, the spectral density is normalized as:

$$\hat{S}_x(\hat{\omega}) = \frac{2S_x(\hat{\omega})}{{x_{rms}}^2/\omega_{ave}}, \text{with} \quad \hat{\omega} = \frac{\omega}{\omega_{ave}} \tag{34}$$

where x denotes a physical quantity and ω_{ave} is always the mean radian frequency of the free-stream velocity spectrum S_{Ub}. As shown in Figure 1(c,d), $S_{\eta\eta}$ appears wider than S_{Ub}, since the depth-decaying of wave orbital velocity is quite significant for higher frequencies. Most spectral energy of S_{Ub} concentrates in the region $0.5 < \omega/\omega_{ave} < 1.5$, which is discretized into about 80 and 40 wavelets with the chosen $\Delta\omega$ for W1 and W2, respectively. This spectrum width is comparable to typical field measurements, e.g. *Madsen et al.* [1993].

To demonstrate that the WCS can accurately generate the intended irregular waves, the measured $u_\infty(t)$ for test W1_sa are compared with the target $u_\infty(t)$ in Figure 2. The measured time series closely follows the target, except for some minor fluctuations possibly due to residual turbulence after Reynolds-averaging. The RMS value of $u_\infty(t)$, 88.36 cm/s, is slightly larger than the target value, 85 cm/s, by 4%. The target $u_\infty(t)$ is essentially the cross-section average velocity $\bar{u}(t)$. Since boundary layers reduce the effective cross-section area of the test channel carrying $\bar{u}(t)$, it is expected that the actual $u_\infty(t)$ should be slightly higher than $\bar{u}(t)$ or the target $u_\infty(t)$. The normalized velocity spectra shown in Figure 2a are virtually identical, suggesting that the intended S_{Ub} is perfectly produced, despite of the 4% difference in $U_{\infty,rms}$. Therefore, it is concluded that the WCS can very precisely generate the intended irregular waves. Since the time series of $u_\infty(t)$ is selected with minimum nonlinear feature, the observed mean velocity (averaged over one recurrence period) for wave-alone tests are virtually zero (of the order 1 mm/s), indicating no turbulence asymmetry streaming for wave-alone tests.

Currents in the WCS are specified by the working frequency f_p of the rotary-lobe pump. In this study we consider two currents with f_p=13 Hz and 26 Hz, which have cross-section average current velocities of 15 cm/s and 30 cm/s, respectively. Preliminary tests of currents in the presence of the two irregular waves selected in this study suggest that reversing the current direction has negligible effect on the current velocity profile, which demonstrates the "symmetry" of the wave flows or the absence of turbulence asymmetry streaming. Given that progressive wave streaming is also absent in OWTs, any observed effects of waves on currents should be purely due to the basic wave-current interaction.

Table 1 summarizes the key parameters for all tests performed in this study. The wave condition is specified by $U_{\infty,rms}$ and T_{ave} of the measured free-stream velocity. The current condition is specified by a reference current velocity u_c measured at a reference level z_r, which is chosen to be z_r =10 cm (following YM15). The current and wave shear velocities, u_{*c} and u_{*w} (defined in Equation (19)), are obtained from the measurements of bottom shear stress (see section 4.4.1). The selected two current conditions have ratios of u_{*c}/u_{*w} generally in the range 0.3 to 0.6, so the currents can be considered weaker than the waves for all tests in this study. For turbulent flows over a rough bottom, the pioneering work by *Nikuradse* [1933] suggests that the bottom roughness k_b varies with flow conditions, which is characterized by a roughness Reynolds number $Re_* = u_* k_N/\nu$, where k_N is the equivalent Nikuradse sand grain roughness (YM14 obtained k_N=20mm and 3.7mm for sandpaper and ceramic-marble bottoms, respectively). For sufficiently large Re_*, boundary layer flows are within the fully-rough turbulent regime, and $k_b = k_N$. Here the wave-current shear velocity u_{*cw} defined by Equation (18) is used as the characteristic shear velocity in Re_*, and list the obtained Re_* together with k_b in Table 1. More discussions on the way to obtain k_b and how k_b varies with Re_* will be presented in section 4.1. To test the equivalent-wave concept of M94, equivalent-wave tests, i.e.

replacing the irregular oscillatory flow by a sinusoidal oscillatory flow with amplitude $U_b = U_{\infty,rms}$ and period $T = T_{ave}$, are performed for the 6 tests over the ceramic-marble bottom, and the key details are also summarized in Table 1.

4. Boundary layer flows under irregular waves with or without a current

4.1. Root-mean-square wave velocity

The measured 2D velocity fields are horizontally averaged into Reynolds-averaged velocity profiles $u(z,t)$. For each vertical level $u(z,t)$ is Fourier analyzed to given the velocity spectrum, $S_U(\omega, z)$, which further gives the RMS wave velocity $U_{rms}(z)$. The following discussion on $U_{rms}(z)$ is based on tests with the W1 wave, while same conclusions can be made for tests with the W2 wave.

Figure 3a shows the measured $U_{rms}(z)$ for a typical test W1_cm together with the amplitude of first-harmonic velocity $U_1(z)$ of its equivalent-wave test. The comparison suggests that $U_{rms}(z)$ and $U_1(z)$ have very similar vertical variations. In the region sufficiently far from the bottom, both $U_{rms}(z)$ and $U_1(z)$ are very uniform, indicating the free-stream region. $U_{rms}(z)$ starts to deviate from the free-stream value roughly at the level $z \sim 110$ mm, which is apparently higher than the $z \sim 80$ mm for $U_1(z)$, so the irregular wave boundary layer seems to be thicker than its equivalent periodic wave boundary layer, which will be discussed later in section 4.3. Within the wave boundary layer, both $U_{rms}(z)$ and $U_1(z)$ first increase to about 5-7% higher than their free-stream values and then decreases rapidly toward the bottom to satisfy the no-slip boundary condition, so both profiles exhibit an overshoot structure.

To illustrate the details of $U_{rms}(z)$ in the very near-bottom region, Figure 4 shows the measured $U_{rms}(z)$ in a logarithmic vertical coordinate for W1 waves over the two rough bottoms with or without a superimposed C2 current. It can be clearly seen that $U_{rms}(z)$ nicely follows a logarithmic velocity profile in the region a few millimeters from the bottom, so log-profile fitting analysis is applied to obtain the bottom roughness k_b and the controlling shear velocity u_*. For periodic wave or wave-current boundary layers, the GM model and the experiment results by YM14 and YM15 all demonstrate that the logarithmic approximation is valid for $z/l \ll 1$, where $l = \kappa u_{*cw}/\omega$ is a characteristic boundary layer length scale. To have sufficient (more than 5) data points, $z/l \leq 0.15$ is simply chosen as an upper limit for selecting data points for log-profile fitting analysis, where u_{*cw} in $l = \kappa u_{*cw}/\omega$ is directly obtained from measurements of bottom shear stress (discussed later in section 4.4.1). For all tests in this study, the lowest level for valid PIV measurements (1-2mm above the crests of roughness elements) is outside the laminar sublayer and the buffer layer [*Jiménez*, 2004], so all data points satisfying $z/l \leq 0.15$ are used in the analysis. Figure 4 shows the fitted logarithmic profiles, and Table 3 presents the associated numeric details. The overall quality of log-profile fitting is represented by the coefficient of determination R^2 with $R^2 = 1$ or $1 - R^2 = 0$ indicating a perfect fitting. For the four tests in Figure 4, the value of $1 - R^2$ is of the order $O(10^{-5} \sim 10^{-4})$, suggesting good fitting quality. The confidence level for u_* is represented by the relative 95% confidence interval, $\Delta u_*/u_*$, which is only about 1-5%. The confidence level for bottom roughness k_b is given by a 95% confidence factor $r_{\Delta k} > 1$, i.e. the true k_b is 95%-likely between, $k_b/r_{\Delta k}$ and $k_b \cdot r_{\Delta k}$, and the obtained $r_{\Delta k}$ is between 1.05 and 1.11. These small confidence limits demonstrate that the fitted u_* and k_b are very reliable.

The fitted bottom roughness k_b for all 12 tests are presented in Table 1 together with measured Re_*, which characterizes turbulent conditions. For tests over the ceramic-marble bottom Re_* is of the order 1000, so they are all within the fully-rough turbulent regime, and their k_b (19.9 ± 1.1 mm) is indeed very close to $k_N = 20$ mm. For the sandpaper bottom, YM14 shows that the fully rough turbulent regime is established for $Re_* \geq 300$, so all W1 tests are within the fully rough turbulent regime, as evidence by the fact that their k_b (3.6 ± 0.4 mm) is very close to $k_N = 3.7$ mm, while all W2 tests are within the transient regime, and their k_b is consistently smaller than $k_N = 3.7$ mm. These obtained bottom roughnesses are very close to those for periodic wave, pure-current and period wave-current tests in previous studies (YM14 and YM15), so wave irregularity does not affect the bottom roughness controlling wave boundary layer flows over the same bottom configurations. The difference in fitted k_b between wave-alone and wave-current tests, e.g. the difference between k_b for W1_cm and W1C2_cm, are negligible, which suggests that the roughness experienced by irregular waves are not affected by a superimposed current.

Based on these observations, it is concluded that the RMS velocity of irregular waves indeed behaves as the first-harmonic velocity amplitude of the equivalent periodic wave, as suggested by the M94's equivalent-wave concept.

4.2. Phase-lead of near-bottom velocity

It has been shown that horizontal velocity within periodic wave boundary layers leads the free-stream velocity in time [e.g *Sleath*, 1987], which is also observed for the irregular wave boundary layers in this study. Figure 5 compares the normalized free-stream velocity $u_\infty(t)$ and $u(z,t)$ measured at $z = 4.9$ mm, which represents the near-bottom velocity, for a typical wave-alone test W1_cm. The measurements suggest that $u(z,t)$ closely follows $u_\infty(t)$ with a small time lead Δt. A representative value for Δt is quantified based on the cross-correlation coefficient ρ_{Cr} between $u_\infty(t + \Delta t)$ and $u(z,t)$, i.e. the time lead

Δt gives the ρ_{Cr} closest to 1 is taken as the representative value, and is translated into a representative phase lead based on the average wave period T_{ave} of the free-stream velocity:

$$\varphi_U(z) = \frac{2\pi\Delta t(z)}{T_{ave}} \tag{35}$$

Thus, a vertical profile of representative phase lead $\varphi_U(z)$ is obtained. Figure 3b shows $\varphi_U(z)$ for test W1_cm, and the phase $\varphi_1(z)$ of first-harmonic velocity of its equivalent-wave test is also provided for easy comparison. As the bottom is approached, both $\varphi_U(z)$ and $\varphi_1(z)$ first decrease by slightly about $0.1 \sim 0.2°$ from zero, and then increase to about 25° in the very near-bottom region. Generally speaking, $\varphi_U(z)$ and $\varphi_1(z)$ very closely follow each other, except for the region for 30 mm$< z <$80 mm, where a discrepancy of $1 \sim 2°$ is observed. This observation, together with the observed similarity between RMS wave velocity and its equivalent, support the equivalent-wave concept of M94.

4.3. Characteristic Boundary layer thickness

Many researchers, e.g. YM14, take the elevation of the maximum overshoot of first-harmonic-velocity amplitude as a characteristic boundary layer thickness δ_m for periodic wave boundary layers. YM14 obtained the following empirical formula for δ_m from fitting experimental results:

$$\frac{\delta_m}{k_N} = 0.079\left(\frac{A_b}{k_N}\right)^{0.81} \tag{36}$$

The observations shown in section 4.1 suggest a good similarity between the RMS wave velocity of irregular waves and the first-harmonic-velocity amplitude of periodic waves, so here δ_m is defined as the elevation of the maximum overshoot of the RMS wave velocity. For the four wave-alone tests, the measurements are compared with the predictions given by Equation (36) with A_b being the RMS excursion amplitude $A_{b,rms} = U_{\infty,rms}/\omega_{ave}$. As shown in Figure 6, the measured values for δ_m are consistently higher than the predictions by roughly 18%. Since Equation (36) is obtained based on periodic-wave experiments, the discrepancy suggests that the irregular wave boundary layers are thicker than their equivalent periodic wave boundary layers, which is in agreement with the observation in Figure 3. For a train of irregular waves, previous experimental studies showed that wave boundary layer thickness changes with individual waves [e.g. *Bhawanin et al.*, 2014], since wave boundary layers are re-developed after each flow reversal. Therefore, some very strong individual waves have boundary layers thicker than that of the equivalent periodic wave. The deviation of $U_{rms}(z)$ from the free-stream value at high levels is probably due to these large waves, so the characteristic boundary layer thickness based on $U_{rms}(z)$ appears larger than that of the equivalent periodic wave. However, this 18% difference is negligible if one wants to predict δ_m for moveable sea bottom with Equation (36). This is because the inaccuracy in determining the moveable bottom roughness k_N is much higher than 18%. Thus, δ_m can still be reasonably predicted for irregular waves using the equivalent-wave concept.

4.4. Bottom shear stress

4.4.1. Experimental determination of bottom shear stress

Bottom shear stress in the WCS must be inferred from velocity measurements, and YM14 showed that the log-profile fitting method is the only valid method for rough-bottom tests. This method assumes that the flow is quasi-steady in the very near-bottom region, so the instantaneous velocity profile follows a logarithmic distribution controlled by the instantaneous shear velocity $u_*(t) = \sqrt{|\tau_b(t)|/\rho}$ and physical bottom roughness k_b. Thus, instantaneous bottom shear stress $\tau_b(t)$ can be obtained through log-profile fittings.

This method is not valid around flow reversals, when the effect of adverse pressure gradient invalidates the log-profile approximation, but for most (about 70%) of the time, especially at (or close to) maximum flow conditions, the method works reasonably well. Both $u_*(t)$ and k_b can be taken as unknowns in the log-profile fitting analysis, but YM14 proposed a modified log-profile fitting, which takes a fixed value for k_b, to improve accuracy, and also to be consistent with the assumption of a constant k_b in most analytical models. Thus, we follow YM14 and take the k_b given by fitting the RMS wave velocity profile in the modified log-profile fitting. To ensure that the analysis is in the very near-bottom region and also have enough data points, the bottom-most 5 data points are used (also following YM14). Figure 7 shows the log-profile fitting for three representative instantaneous velocity profiles for test W1_sa. For profiles P1 and P2, the free-stream velocity is close to the local maximum, and the fitted log-profiles nicely approximate the measurements. However, for profile P3, which is slightly before a flow reversal, the near-bottom velocity opposites the free-stream velocity, indicating a flow separation, which has already been observed for periodic wave boundary layer flows [e.g. *Jensen et al.*, 1989]. For such situations, although the modified log-profile fitting cannot give the accurate instantaneous bottom shear stress for P3, it still qualitatively yields a small bottom shear stress in the direction of the instantaneous near-bottom flow, which can be taken as a local interpolation. It should be pointed out that using other interpolation schemes to estimate bottom shear stress around flow reversal has little effect on the following analysis, e.g. the RMS bottom shear stress only varies by 1-2% if a cubic-spline interpolation is applied to “fill the gaps”.

Figure 8 shows a 100-second segment of the obtained instantaneous bottom shear stress together with the free-stream velocity for test W1_sa. Both time series are normalized with their RMS values for easy comparison. The time series of bottom shear stress is reasonably smooth and closely follows the time series of free-stream velocity with a time lead similar to that of the near-bottom velocity (see Figure 5). More discussions on this will be presented in the next subsection.

4.4.2. Bottom shear stress of the equivalent wave and energy dissipation rate

The measured RMS wave bottom shear stress and free-stream velocity give the following wave friction factor defined as by M94:

$$f_{cw} = \frac{2{\tau_{b,rms}}^2}{\rho {U_{\infty,rms}}^2} \tag{37}$$

The equivalent-wave concept suggests that this friction factor can be predicted with the improved GM model, i.e. Equation (20), with $U_{\infty,rms}$ and T_{ave} being the velocity amplitude and wave period. Since all input variables for Equation (20) are readily obtained from measurements, we can validate this formula against our measurements. As shown in Figure 9a, the model reasonably predicts f_{cw} for the wave-alone tests (open circles), but gives a slight (less than 10%) overestimate for the wave-current tests (full circles), which are in agreement with the model validations for the equivalent-wave tests (more validations for periodic-wave scenarios can be found in YM14 and YM15). As claimed by YM15, a 10% error in bottom shear stress is usually insignificant compared with other model uncertainties, e.g. the determination of movable bottom roughness, so applying the equivalent-wave concept with the improved GM model can accurately predicted the RMS wave bottom shear stress.

As shown in Figure 8, bottom shear stress leads the free-stream velocity in time. The significance of this time lead lies in that it influences the energy dissipation rate due to wave bottom shear stress, which is defined as [following *Kajiura*, 1968]:

$$\dot{E} = < \tau_b(t) u_\infty(t) > \quad (38)$$

where the bracket indicates time-averaging. M94 obtained an analytical approximation for $\dot{E}$ under irregular waves as follows. Expressing both $\tau_b(t)$ and $u_\infty(t)$ as summations of infinitesimal wave components, $\dot{E}$ can be written as:

$$E = \sum_n < u_{\infty,n} \cos(\omega_n t) \tau_{bn} \cos(\omega_n t + \varphi_{\tau n}) > \quad (39)$$

where $\varphi_{\tau n}$ is the phase lead of τ_{bn} over $u_{\infty,n}$. For small bottom roughness $\varphi_{\tau n}$ is a weak function of ω_n, and therefore can be replaced by the value φ_τ for $\omega = \omega_{ave}$. After examining the behavior of function $K(\omega_n)$ in Equation (10), the n-th component of bottom shear stress τ_{bn} can be approximately written as:

$$\tau_{bn} \approx \frac{1}{2} f_{cw} \rho u_{\infty,n} U_{\infty,rms} \quad (40)$$

Therefore, $\dot{E}$ is obtained as:

$$\dot{E} = < \tau_b(t) u_\infty(t) > = \frac{1}{2} \tau_{b,rms} U_{\infty,rms} \cos(\varphi_\tau) \quad (41)$$

Using measurements of $\tau_b(t)$ and $u_\infty(t)$, we can directly evaluate $\dot{E}$ with Equation (38), so φ_τ can be obtained through:

$$\cos(\varphi_\tau) = 2 \frac{\dot{E}}{\tau_{b,rms} U_{\infty,rms}} \quad (42)$$

Alternatively, we can estimate $\varphi_\tau = \omega_{ave} \Delta t$ using the cross-correlation analysis between $\tau_b(t)$ and $u_\infty(t)$ to obtain the Δt maximizing the cross-correlation coefficient. Thus, we can validate the improved GM model, i.e. Equation (22), against the measurements obtained in two different approaches. As shown in Figure 9b, both the two groups of measurements and the model suggest that φ_τ decreases with the parameter $C_\mu A_b / k_b$. φ_τ

obtained from cross-correlation analysis (circles) is constantly smaller than φ_τ obtained based on dissipation rate (squares) by about $5 \sim 10^\circ$. The model predictions are lower than the measurements based on dissipation rates by less than 5°. Such a discrepancy will lead to less than 5% overestimate for the prediction of energy dissipation rate, since $\cos(\varphi_\tau)$ varies slowly with φ_τ in the range $5^\circ < \varphi_\tau < 30^\circ$. It should be point out that the dissipation-rate approach is very sensitive to the determination error in $\tau_{b,rms}$ and $U_{\infty,rms}$, i.e. reducing one of them by 1% will lead to $1 \sim 2^\circ$ reduction in the obtained φ_τ. Since both $\tau_{b,rms}$ and $U_{\infty,rms}$ contain residual turbulence, their actual values should be smaller, and hence φ_τ is very-likely overestimated by a few degrees. Thus, although the comparison suggests the model may have certain bias, the associated error is generally negligible.

Some researchers [e.g. *Jonsson*, 1966] proposed the following temporal variation of bottom shear stress for periodic waves:

$$\tau_b(t) \propto |\cos(\omega t)| \cos(\omega t) \tag{43}$$

By assuming that $\dot{E}$ of irregular waves is the same as $\dot{E}$ of the equivalent periodic wave and adopting Equation (43) for $\tau_b(t)$, another estimate of $\dot{E}$ is:

$$\dot{E} = \frac{4}{3\pi} \tau_{b,rms} U_{\infty,rms} \cos(\varphi_\tau) \tag{44}$$

This formula for energy dissipation rate is adopted in many studies with or without considering the phase-lead effect ($\cos\varphi_\tau$), e.g. *Traykovski et al.* [2015] used it for analyzing field data. However, the equivalent-wave analogy embedded in Equation (44) is purely hypothetical, while Equation (41) is analytically derived. In fact, Equation (42) will always give a $\cos(\varphi_\tau) \geq 1$ for all tests in this study if the factor 2 is changed to $3\pi/4$, indicating that Equation (44) underestimates the energy dissipation rate even with $\cos\varphi_\tau$ neglected. This finding can be considered as an experimental evidence to support Equation (41) over Equation (44) for predicting $\dot{E}$.

4.5. Spectral analysis

To facilitate the comparison among velocity spectra at different vertical levels, the velocity spectrum at level z is normalized with the local RMS wave velocity $U_{rms}(z)$ and the average radian frequency ω_{ave} of the free-stream velocity, as defined by Equation (34). Figure 10(a,b) compares the normalized spectra of the free-stream velocity and the velocity measured at z =4.9 mm (the bottom-most level for valid PIV measurements) for test W1_cm (wave-alone) and test W1C2_cm (wave-current) over the ceramic-marble bottom. The irregular waves for both tests have a target $U_{\infty,rms}$ of 0.85 m/s and a target T_{ave} of 6.25 s. The spectrum at z =4.9 mm exhibits slightly larger data scatter than the free-stream one, which is possibly due to the stronger residual turbulence after Reynolds-averaging in the near-bottom region, but the difference between the two normalized spectra can still be considered negligible. If we closely inspect the measurements, we can see that for the low-frequency regime, $\omega/\omega_{ave} \leq 1$, the normalized spectral density of the near-bottom velocity is slightly lower than that of the free-stream velocity, while the opposite occurs for the high-frequency regime $\omega/\omega_{ave} \geq 1$. This can be explained by the behavior of function $F(\omega_n, z)$ in Equation (9), i.e. $|F(\omega, z)|^2 < 1$ generally increases with ω in the near-bottom region, leading to less reduction in spectral density for higher frequencies. Nevertheless, the closeness between the two normalized spectra indicates that the velocity spectrum at a given vertical level z is proportional to the free-stream velocity spectrum with a factor $(U_{rms}(z)/U_{\infty,rms})^2$, which is essential for theoretically deriving the equivalent-wave concept.

Figure 10(c,d) shows the normalized spectra of bottom shear stress $S_{\tau b}(\omega)$ for tests W1_cm and W1C2_cm. The normalized spectra for free-stream velocity $S_{Ub}(\omega)$ are also provided for easy comparison. The normalized $S_{\tau b}(\omega)$ closely follows the normalized $S_{Ub}(\omega)$ for both tests, suggesting that $S_{\tau b}(\omega)$ is also proportional to $S_{Ub}(\omega)$, as predicted by M94. Since bottom shear stress is obtained by log-profile fitting the near-bottom velocity, of which the spectrum is already shown to be proportional to $S_{Ub}(\omega)$, it is actually expected to see that $S_{\tau b}(\omega) \propto S_{Ub}(\omega)$. The comparisons between Figure 10(a,b) and (c,d) suggest that the co-existing current do not affect the shape of the spectra.

An interesting observation is that there is a secondary peak in the spectrum of bottom shear stress for wave-alone tests in the frequency range $\omega/\omega_{ave} = 3$. As shown in Figure 11 for test W1_cm, despite of the noticeable scatter, the spectral density around $\omega/\omega_{ave} = 3$ is significantly higher than the background noise, and is about 1% of the spectral density of the primary peak around $\omega/\omega_{ave} = 1$. For periodic wave boundary layers, YM14 shows that the bottom shear stress can be considered as the superposition of a primary first harmonic and a secondary third harmonic:

$$\tau_b(t) = \tau_{b1}\cos(\omega t) + \tau_{b3}\cos(3\omega t) \tag{45}$$

The third harmonic is roughly 15% of the first harmonic in amplitude, or 2% in energy. Thus, the observed secondary peak around $\omega/\omega_{ave} = 3$ is equivalent to the third-harmonic bottom shear stress for periodic waves. *Trowbridge and Madsen* [1984a] adopted a time-varying turbulent eddy viscosity and showed that the third-harmonic bottom shear stress for periodic waves is produced by the interaction of the first-harmonic velocity and the second-harmonic turbulent eddy viscosity. Thus, this observed secondary peak should be explained by similar physics, which is not captured by the time-invariant turbulent eddy viscosity in the M94 model.

5. Current in the presence of irregular waves

The current velocity and current bottom shear stress are obtained by averaging the instantaneous velocity and bottom shear stress over the entire recurrence period of a wave-current test.

5.1. Typical current velocity profile in the presence of irregular waves

Figure 12 shows the current velocity profile with a logarithmic vertical coordinate for a typical test W1C2_sa (current with a roughly 30 cm/s average velocity in the presence of irregular waves with $U_{\infty,rms} = 0.85$ m/s and $T_{ave} = 6.25$ s over the sandpaper bottom). The measurements clearly follow the two-log-profile structure suggested by the M94 model, i.e. Equation (16). The lower current velocity profile is steeper than the upper current velocity profile, indicating a reduced shear velocity, i.e. $u_{*c1}/u_{*c2} = u_{*c}/u_{*cw} < 1$ in Equation (16).

To perform log-profile fitting analysis, the data selection rule proposed YM15 for periodic wave-current boundary layer is adopted here. For the lower current velocity profile, which should be within the wave boundary layer, we simply apply the data-selection limits for fitting the RMS wave velocity profile (see section 4.1). For the upper current velocity profile, the data within the following range is selected for log-profile fitting:

$$1.5\delta_{ct} < z < 10\text{cm} \tag{46}$$

where δ_{ct} in the lower limit is the beginning of the upper logarithmic current profile suggested by the improved GM model, which can be be evaluated using Equations (A2) to (A4) with experimental values of A_b/k_b and $\alpha = u_{*c}/u_{*cw}$. The 1.5 factor in the lower limit is to account for the uncertainty in δ_{ct}. The current in the WCS is driven by a mean pressure gradient, which is neglected in the improved GM model based on the near-wall argument. However, YM15 estimated that this mean pressure gradient does not invalidate the upper logarithmic current profile for $z < 10$ cm, so $z = 10$ cm is taken as an upper limit for data selection. The fitted logarithmic profiles are shown in Figure 12, and the numeric details are presented in Table 4. The measurements nicely follow the fitted profiles, which is reflected by the very low value of $1 - R^2$ and very small confidence limits for both fitted shear velocity and bottom roughness.

The bottom roughness controlling the lower current velocity profile is 4.7 mm, which is fairly close to the equivalent Nikuradse sand grain roughness $k_N = 3.7$ mm for the sandpaper bottom. Thus, the lower current velocity profile is shown to be controlled by the physical bottom roughness. Moreover, this obtained bottom roughness is also very close to the bottom roughness $k_b = 4.0$ mm controlling the RMS wave velocity profile (see Table 3), indicating that the same no-slip boundary condition, i.e. $z = 0$ at $z = k_b/30$, can be applied for co-existing irregular waves and currents, which is usually adopted by theoretical models. The bottom roughness for the upper current profile, $k_b = 58.6$ mm, is much larger than the physical bottom roughness, which is in agreement with the important implication of GM model that currents are controlled by a large apparent roughness outside the wave boundary layer.

Before validating the improved M94 model against our measurements, here the measured current velocity profiles in the presence of irregular waves are first compared with their equivalent periodic waves to test the equivalent-wave concept. For the equivalent-wave tests, the sinusoidal oscillatory flows in the WCS take the RMS free-stream velocity and average period of their corresponding irregular oscillatory flows as their velocity amplitude and wave period, respectively, and the equivalence for currents is achieved by keeping the pump's working frequency (or total discharge). Figure 13 compares the measured current profiles for two representative tests W1C1_cm (relatively weak current or low u_{*c}/u_{*w}) and W2C2_cm (relatively strong current or high u_{*c}/u_{*w}). The two current profiles are very close to each other in the very near-bottom region, where the lower logarithmic current profile exists, but in the transition region the current profiles with the periodic equivalent wave seem to curve slightly more than the ones with irregular waves, and therefore a small difference for the upper current logarithmic profile is observed, i.e. the current velocity with the periodic equivalent wave is slightly higher by a few percentage. Nevertheless, the difference can be considered immaterial, so it is experimentally demonstrated that the basic wave-current interaction can be represented with the equivalent-wave concept.

5.2. Modeling wave-current interaction using the representative-wave concept

In this subsection, the improved M94 model is validated against the wave-current tests in this study. For this model, the inputs for wave conditions are the measured RMS free-stream wave velocity $U_{\infty,rms}$ and average period T_{ave}. Following YM15, the current condition is specified by the measured current velocity at a reference level $z_r = 10$ cm. It should be noted that the choice of reference level has negligible effect on predictions, as long as z_r is within the region of upper logarithmic current profile. For tests within the fully-rough turbulent regime, $k_b = k_N$ is adopted as bottom roughness, while for the W2 tests over the sandpaper bottom, k_b given by fitting the RMS wave velocity profile is used in predictions.

Figure 14 compares the predicted and measured current velocity profiles for the four tests with the W1 wave condition. The improved M94 model very accurately predicts the upper current velocity profile, while the prediction for the lower current velocity profile deviates from the measurements a bit by less than 10%. The sharp kink in predictions should not be considered as model inaccuracy, as it is due to the discontinuity of the bi-linear turbulent eddy viscosity, which is kept in the improved M94 model for simplicity. The predictions of two key parameters, current shear velocity u_{*c} and apparent roughness k_{Na}, are further validated against measurements. As shown in Figure 15a, the improved M94 model slightly overestimates u_{*c} by 6.6%, which is in agreement with the inaccuracy for periodic wave-current boundary layers (see YM15). The comparison for apparent roughness exhibits larger scatter (Figure 15b), i.e. the difference between predictions and measurements varies between 10 to 30%, but the overall agreement is a factor of 1.032. Thus, in terms of these two key parameters the model performance is also excellent.

6. Summary and discussion

A full-scale experimental study of irregular wave boundary layers with or without a superimposed current is conducted in an oscillatory water tunnel. Tests include two wave conditions and two current conditions over two fixed rough bottoms with well-known physical roughness and theoretical bed level. Boundary layer flows are measured using a 2D PIV system, and the measured instantaneous velocity fields are horizontally averaged to give Reynolds-averaged velocity profiles. Instantaneous bottom shear stress is estimated by log-profile fitting the instantaneous velocity profiles in the very near-bottom region, which is found to follow the logarithmic law during most of the time.

To generate realistic prototype flow conditions, the free-stream velocity spectrum is given by the spectrum of wave bottom velocity under conceptual irregular surface waves described by the JONSWAP spectrum. Time series of free-stream velocity is generated by superimposing a large number of wave components with randomly assigned phases, which form a discretization of the free-stream velocity spectrum. Since this study focuses on the basic wave-current interaction, the generated time series with negligible nonlinear features, i.e. almost no skewness in velocity and acceleration, are selected for experiments.

The RMS wave velocity profile and the representative velocity phase lead for irregular wave boundary layers are very similar to the amplitude and phase of first-harmonic velocity for the corresponding equivalent periodic waves. The RMS wave velocity closely follows the logarithmic velocity profile in the very near bottom region, which is controlled by the physical bottom roughness. Based on a characteristic boundary layer thickness, i.e. the elevation of maximum overshoot of the RMS wave velocity profile, the irregular wave boundary layers appear slightly "thicker" than the equivalent periodic wave boundary layers. This is possibly due to the large waves in a package of irregular waves, which have thicker boundary layers.

The wave friction factor, which represents the RMS wave bottom shear stress, can be accurately predicted by the improved M94 model for wave-alone and wave-current tests. A representative phase lead of bottom shear stress over the free-stream velocity can be obtained by either correlation analysis or by considering wave energy dissipation rate. The dissipation-rate approach yields a phase lead $5 \sim 10^\circ$ larger than the correlation approach, while the prediction by the improved M94 model is generally between the two measurements. The bottom-shear-stress spectrum and the velocity spectra within the wave boundary layer are found to be proportional to the free-stream velocity spectrum, which is essential for theoretically deriving the equivalent-wave concept. A small but meaningful secondary peak is observed in the high-frequency range of bottom shear stress spectrum for pure wave tests, which is possibly produced by the same physics leading to a third-harmonic bottom shear stress under sinusoidal oscillatory flows.

Currents in the presence of irregular waves exhibit the classic two-log-profile structure suggested by the periodic-wave-based GM model. The lower log-profile is controlled by the physical bottom roughness, while the upper log-profile is controlled by a much larger apparent roughness, which characterizes the effect of waves on currents. Little difference is observed between the measured current velocity profiles in the presence of irregular waves and the corresponding equivalent sinusoidal wave, which experimentally supports the equivalent-wave concept. The improved M94 model is validated against measurements for predicting current velocity profiles. The predicted current velocity profiles, as well as the current shear velocity and apparent roughness, are all in good agreement with measurements.

This study together with YM14 and YM15, form a group of experimental studies, which are comparable to the studies of *Mathisen and Madsen* [1996a, b, 1999] (MM hereafter), i.e. both groups consider periodic and irregular waves with or without collinear currents over fixed rough bottom configurations. The general conclusions for both groups are similar: (a) a single bottom roughness of a fixed rough bed can be applied for waves and currents and (b) the wave-current interaction can be modeled accurately with the

GM-type model for periodic waves and M94-type model for irregular waves. However, there is a fundamental difference between the two groups, which is primarily due to the value of bottom roughness. In MM's study, the bottom roughness has to be very large to ensure turbulent flow conditions, so the near-bottom wave excursion amplitude in their study is smaller than the physical bottom roughness, i.e. $A_b/k_b < 1$. Their observations also suggest that the wave boundary layer thickness δ is comparable to A_b, and therefore smaller than k_b. Thus, their experiments are actually outside the limits of validity for both GM or M94 models (as acknowledged by the authors), since both models assume $k_b \ll \delta \ll A_b$ for applying the no-slip boundary condition at $z = z_0 = k_b/30$ and linearizing the governing equation. Consequently, the actual wave boundary layers in their study should be dramatically different from those suggested by the two models. Nevertheless, by extrapolating the GM or M94 models outside their limits of validity, MM back-calculated bottom roughness for waves based on measured wave attenuation and the bottom roughness for currents in the presence of waves based on measured current velocity profile. The obtained values of bottom roughness are reasonably close to the physical bottom roughness obtained from log-profile fitting pure current logarithmic profiles. This suggests that for the low A_b/k_b regime wave-current boundary layers can still be reasonably modeled with the GM or M94 models and the physical bottom roughness, even though the models are completely conceptual. Thus, to some extent, the MM's work does not directly validate both models, but shows that they can be applied for large roughness value with the same accuracy as their experiments. In this study, however, the assumption of $k_b \ll \delta \ll A_b$ is valid, due to large values of A_b/k_b, so the wave boundary layer suggested by the two models indeed exists. The bottom roughness experienced by waves is therefore directly obtained from log-profile fitting the RMS wave velocity. Comparing to MM's work, this work, together with YM14 and YM15, give a direct experimental validation of the GM and M94 models. For field conditions with a moveable seabed, large values of A_b/k_b occur in the sheet-flow regime, while low values of A_b/k_b occur in the ripple-bed regime. Thus, the two groups of experimental work to some extent separately validate the GM and M94 models for these two regimes of moveable bed.

This study is directly aimed at investigating the basic wave-current interaction under irregular waves, so the flow conditions closely follow the approximations of M94 model, i.e. longitudinal flow homogeneity and no nonlinear feature in the free-stream wave velocity. Therefore, the effect of both progressive-wave streaming and turbulence-asymmetry streaming are excluded in this study. Also, all experiments have collinear waves and currents, while some evidences suggest that the GM model, which is embedded in the M94 model, may not work so well for waves and currents at an angle as for collinear wave-current flows. Nevertheless, this study provides a foundation for future research on the effect of these limitations. The most straightforward extension to this work is adding some features of wave nonlinearity, i.e. skewness in velocity or acceleration, to the irregular oscillatory flows. In fact, we have done preliminary studies and indeed observed the turbulence-asymmetry streaming under irregular waves, and more investigations are underway.

Appendix A: Improved Grant-Madsen Model for periodic wave-current boundary layer

The original GM model, which is embedded in M94, adopts a discontinuous bi-linear structure for turbulent eddy viscosity ν_T with a rather arbitrarily-defined transition level

δ_{cw}. Meanwhile, the wave boundary layer is solved with only considering the lowest layer of ν_T, i.e. $\nu_T = \kappa u_{*cw} z$, so the obtained wave friction factor (or wave bottom shear stress) may be inaccurate. *Humbyrd* [2012] modified the GM model by adopting a three-layer continuous structure for ν_T:

$$\nu_T = \begin{cases} \kappa u_{*cw} z & z_0 < z \leq \delta_t \\ \kappa u_{*cw} \delta_t & \delta_t < z \leq \delta_{ct} \\ \kappa u_{*c} z & \delta_{ct} \leq z \end{cases} \tag{A1}$$

Inside the wave boundary layer, ν_T is scaled with the wave-current shear velocity u_{*cw} based on the maximum bottom shear stress, and has a linear-constant structure, which gives the lowest two layers. The first transition level δ_t is taken as 1/6 of the wave boundary layer thickness: $\delta_t = \delta_w/6$, where δ_w is defined as the level where the wave velocity deficit reaches 5% of the free-stream value and is obtained by iteratively solving the wave equation. *Humbyrd* [2012] provided an approximate explicit formula for δ_w:

$$\frac{\delta_w}{l} = \exp\left\{ a(C_\mu \frac{A_{bm}}{k_b})^b + c \right\} \tag{A2}$$

where $l = \kappa u_{*cw}/\omega$ is a characteristic wave boundary layer scale and:

$$C_\mu = (1 - \alpha^2)^{-1} \tag{A3}$$

with $\alpha = u_{*c}/u_{*cw}$. The parameters, a, b, and c are also given by explicit formulas of α, which are provided in YM15. The second transition level is where the turbulent eddy viscosity $\nu_T = \kappa u_{*c} z$ intersects with $\nu_T = \kappa u_{*m} \delta_t$:

$$\delta_{ct} = \frac{1}{6} \frac{u_{*cw}}{u_{*c}} \delta_w \tag{A4}$$

With this three-layer structure for ν_T, the predicted current velocity profile is two logarithmic profiles connected by a smooth transition. To translate this into the simple two-log-profile structure suggested by the original GM model, the intersection of the top and bottom logarithmic profiles is obtained, which can be expressed as:

$$\frac{\delta_{cw}}{l} = \frac{\delta_w}{16.3}\alpha^{\left(\frac{1}{\alpha-1}\right)}/l = f(\alpha) \tag{A5}$$

Thus, the original GM model can be simply improved by adopting this as the transition level for the bi-linear turbulent eddy viscosity.

Unlike the GM and M94 models, *Humbyrd* [2012] solved the wave equation with the entire vertical structure of turbulent eddy viscosity, so the effect of currents on waves are captured more precisely and the predicted wave bottom shear stress is more accurate. The reader is referred to YM15 for model performances for periodic wave-current boundary layers.

Acknowledgments. The author gratefully acknowledges the financial support from the start-up grant of National University of Singapore (R-302-000-089-133)and the Open Research Fund Program of State key Laboratory of Hydroscience and Engineering of Tsinghua University. The author also thanks the CENSAM program for Singapore-MIT Alliance for Research and Technology (SMART) for providing the experimental facilities.

References

Abramowitz, M., and I. A. Stegun (1965), *Handbook of mathematical functions*, Dover Publications.

Afzal, M. S., L. E. Holmedal, and D. Myrhaug (2015), Three-dimensional streaming in the seabed boundary layer beneath propagating waves with an angle of attack on the current, *Journal of Geophysical Research: Oceans*, *120*(6), 4370–4391.

Berni, C., E. Barthélemy, and H. Michallet (2013), Surf zone cross-shore boundary layer velocity asymmetry and skewness: An experimental study on a mobile bed, *Journal of Geophysical*

Research: Oceans, *118*(4), 2188–2200.

Bhawanin, M., T. O'Donoghue, D. A. van der A and J. S. Ribberink (2014), Effect of flow irregularity on oscillatory boundary layer flow, *Proceedings of the 34th International Conference on Coastal Engineering*, p. sediment. 44.

Blondeaux, P., G. Vittori, A. Bruschi, F. Lalli, and V. Pesarino (2012), Steady streaming and sediment transport at the bottom of sea waves, *Journal of Fluid Mechanics*, *697*, 115–149.

Dally, W. R. (1992), Random breaking waves: Field verification of a wave-by-wave algorithm for engineering application, *Coastal Engineering*, *16*(4), 369–397.

Drake, D. E., and D. A. Cacchione (1992), Wave-current interaction in the bottom boundary layer during storm and non-storm conditions: observations and model predictions, *Continental Shelf Research*, *12*(12), 1331–1352.

Graber, H. C. (1984), Wind wave model for arbitrary water depth, Ph.D. thesis, Massachusetts Institute of Technology, Cambridge, MA, U.S.

Grant, W. D., and O. S. Madsen (1979), Combined wave and current interaction with a rough bottom, *Journal of Geophysical Research: Oceans*, *84*(C4), 1797–1808, doi: 10.1029/JC084iC04p01797.

Grasmeijer, B. T., and B. G. Ruessink (2003), Modeling of waves and currents in the nearshore parametric vs. probabilistic approach, *Coastal Engineering*, *49*(3), 185–207.

Hasselmann, K., T. Barnett, E. Bouws, H. Carlson, D. Cartwright, K. Enke, J. Ewing, H. Gienapp, D. Hasselmann, and P. Kruseman (1973), Measurements of wind-wave growth and swell decay during the joint north sea wave project (JONSWAP), *Tech. rep.*, Deutches Hydrographisches Institut.

Holmedal, L. E., and D. Myrhaug (2009), Wave-induced steady streaming, mass transport and net sediment transport in rough turbulent ocean bottom boundary layers, *Continental Shelf Research*, *29*(7), 911–926.

Holmedal, L. E., D. Myrhaug, and H. Rue (2003), The sea bed boundary layer under random waves plus current, *Continental Shelf Research*, *23*(7), 717–750.

Holmedal, L. E., J. Johari, and D. Myrhaug (2013), The seabed boundary layer beneath waves opposing and following a current, *Continental Shelf Research*, *65*, 27–44.

Humbyrd, C. J. (2012), Turbulent combined wave-current boundary layer model for application in coastal waters, Master's thesis, Massachusetts Institute of Technology, Cambridge, MA, U.S.

Jensen, B. L. and Sumer, B. M. and Fredsøe, J. (1989), Turbulent oscillatory boundary layers at high reynolds numbers, *Journal of Fluid Mechanics*, *206*, 265–297.

Jiménez, J. (2004), Turbulent flows over rough walls, *Annual Review of Fluid Mechanics*, *36*(1), 173–196.

Jonsson, I. G. (1966), Wave boundary layer and friction factors, in *Proceedings of the 10th International Conference on Coastal Engineering*, pp. 127–148, ASCE.

Kajiura, K. (1968), A model of bottom boundary layer in water waves, *Bull. Earthquake Res. lnst., Univ. Tokyo*, *46*, 75–123.

Kitaigordskii, S. A., V. P. Krasitskii, and M. M. Zaslavskii (1975), On phillips' theory of equilibrium range in the spectra of wind-generated gravity waves, *Journal of Physical Oceanography*, *5*(3), 410–420.

Klopman, G. (1994), Vertical structure of the flow due to waves and current, *Prog. Rep. H840.30, Delft Hydraulics*, Delft, Netherlands.

Kranenburg, W. M., J. S. Ribberink, R. E. Uittenbogaard, and S. J. M. H. Hulscher (2012), Net currents in the wave bottom boundary layer: On waveshape streaming and progressive wave streaming, *Journal of Geophysical Research: Earth Surface*, *117*(F3), doi: 10.1029/2011JF002070.

Longuet-Higgins, M. S. (1953), Mass transport in water waves, *Philosophical Transactions of the Royal Society of London. Series A, Mathematical and Physical Sciences*, *245*(903), 535–581.

Madsen, O. S. (1994), Spectral wave-current bottom boundary layer flows, *Proceedings of the 24th International Conference on Coastal Engineering*, pp. 384–398.

Madsen, O. S., Y.-K. Poon, and H. C. Graber (1988), Spectral wave attenuation by bottom friction: theory, *Proceedings of the 21th International Conference on Coastal Engineering*, pp. 492–504.

Madsen, O. S., L. D. Wright, J. D. Boon, and T. A. Chisholm (1993), Wind stress, bed roughness and sediment suspension on the inner shelf during an extreme storm event, *Continental Shelf Research*, *13*(11), 1303–1324.

Mathisen, P. P., and O. S. Madsen (1996a), Waves and currents over a fixed rippled bed: 1. bottom roughness experienced by waves in the presence and absence of currents, *Journal of Geophysical Research: Oceans*, *101*(C7), 16,533–16,542, doi:10.1029/96JC00954.

Mathisen, P. P., and O. S. Madsen (1996b), Waves and currents over a fixed rippled bed: 2. bottom and apparent roughness experienced by currents in the presence of waves, *Journal of Geophysical Research: Oceans*, *101*(C7), 16,543–16,550, doi:10.1029/96JC00955.

Mathisen, P. P., and O. S. Madsen (1999), Waves and currents over a fixed rippled bed: 3. bottom and apparent roughness for spectral waves and currents, *Journal of Geophysical Research: Oceans*, *104*(C8), 18,447–18,461, doi:10.1029/1999JC900114.

Myrhaug, D., L. E. Holmedal, R. R. Simons, and R. D. MacIver (2001), Bottom friction in random waves plus current flow, *Coastal Engineering*, *43*(2), 75–92.

Nayak, A. R., C. Li, B. T. Kiani, and J. Katz (2015), On the wave and current interaction with a rippled seabed in the coastal ocean bottom boundary layer, *Journal of Geophysical Research: Oceans*, *120*(7), 4595–4624.

Nikuradse, J. (1933), Strömungsgesetze in rauhen rohren, *Ver. Dtsch. Ing. Forsch.*, *361*.

O'Donoghue, T., J. S. Doucette, J. J. van der Werf, and J. S. Ribberink (2006), The dimensions of sand ripples in full-scale oscillatory flows, *Coastal Engineering*, *53*(12), 997–1012.

Ribberink, J. S., and A. A. Al-Salem (1995), Sheet flow and suspension of sand in oscillatory boundary layers, *Coastal Engineering*, *25*(3-4), 205–225.

Russell, R. C. H., and J. D. C. Osorio (1958), An experimental investigation of drift profiles in a closed channel, *Coastal Engineering Proceedings*, *1*(6), 10.

Simons, R. R., T. J. Grass, W. M. Saleh, and M. M. Tehrani (1994), Bottom shear stresses under random waves with a current superimposed, *Proceedings of the 24th International Conference on Coastal Engineering*, pp. 565–578.

Sleath, J. F. A. (1987), Turbulent oscillatory flow over rough beds, *Journal of Fluid Mechanics*, *182*, 369–409.

Tanaka, H., and M. A. Samad (2006), Prediction of instantaneous bottom shear stress for smooth turbulent bottom boundary layers under irregular waves, *Journal of Hydraulic Research*, *44*(1), 94–106.

Traykovski, P., J. Trowbridge, and G. Kineke (2015), Mechanisms of surface wave energy dissipation over a high-concentration sediment suspension, *Journal of Geophysical Research: Oceans*, *120*(3), 1638–1681.

Trowbridge, J., and O. S. Madsen (1984a), Turbulent wave boundary layers: 1. model formulation and first-order solution, *Journal of Geophysical Research: Oceans*, *89*(C5), 7989–7997, doi: 10.1029/JC089iC05p07989.

Trowbridge, J., and O. S. Madsen (1984b), Turbulent wave boundary layers: 2. second-order theory and mass transport, *Journal of Geophysical Research: Oceans*, *89*(C5), 7999–8007, doi:10.1029/JC089iC05p07999.

Yuan, J., and O. S. Madsen (2010), On the choice of random wave simulation in the surf zone, *Proceedings of the 32th International Conference on Coastal Engineering*, p. waves.71.

Yuan, J., and O. S. Madsen (2014), Experimental study of turbulent oscillatory boundary layers in an oscillating water tunnel, *Coastal Engineering*, *89*, 63–84.

Yuan, J., and O. S. Madsen (2015), Experimental and theoretical study of wavecurrent turbulent boundary layers, *Journal of Fluid Mechanics*, *765*, 480–523.

Yuan, J., and O. S. Madsen (2015), Experimental and theoretical study of wavecurrent turbulent boundary layers, *Journal of Fluid Mechanics*, *765*, 480–523.

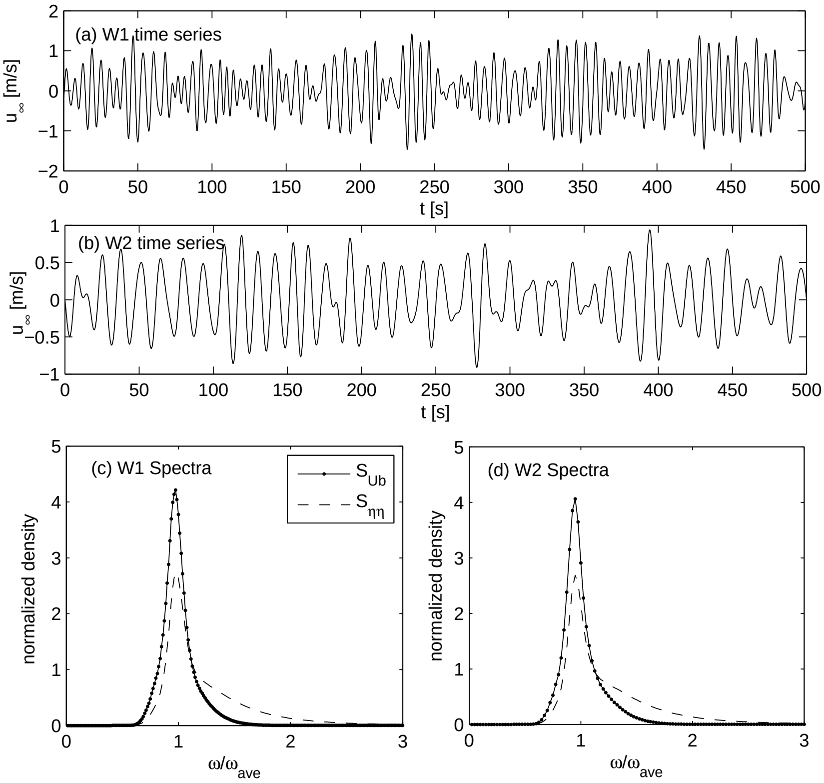

Figure 1. Target wave conditions (a) time series of W1, (b) time series of W2, (c) normalized spectra of W1, (d) normalized spectra of W2.

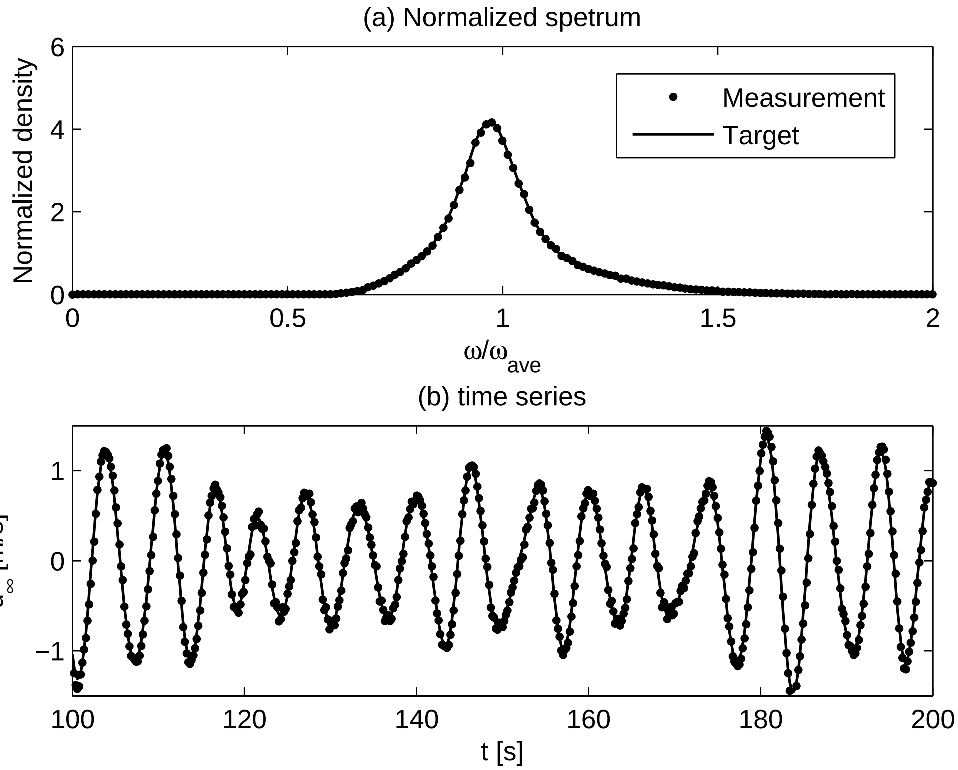

Figure 2. PIV measurements of free-stream velocity for test W1_sa: (a) normalized spectrum, (b) a segment of time series (dots: measurements, solid lines: targets).

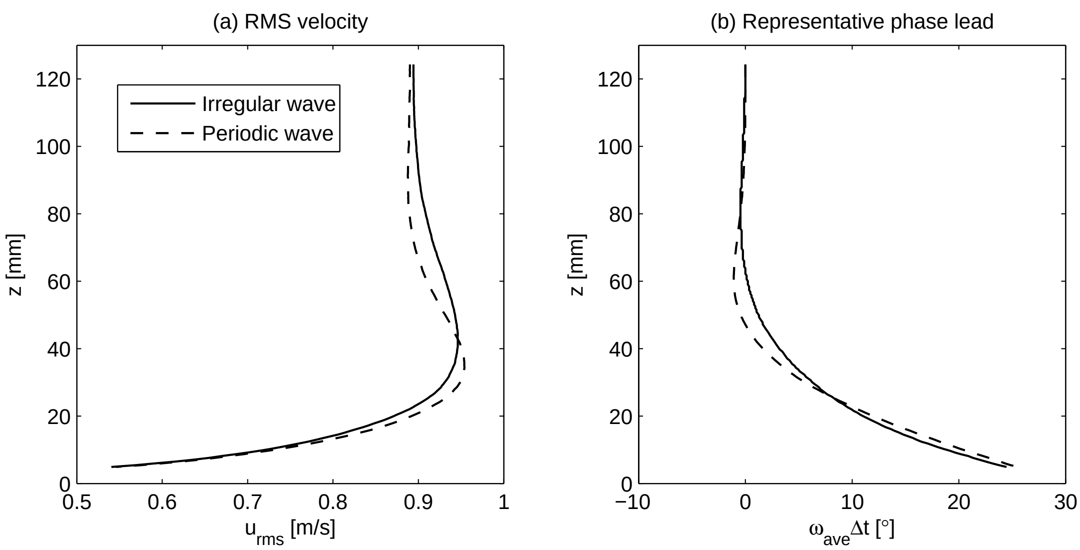

Figure 3. RMS wave velocity and representative phase lead of wave velocity given by correlation analysis for test W1_cm (the dashed lines are the measured amplitude and phase of first-harmonic velocity from the equivalent-wave test

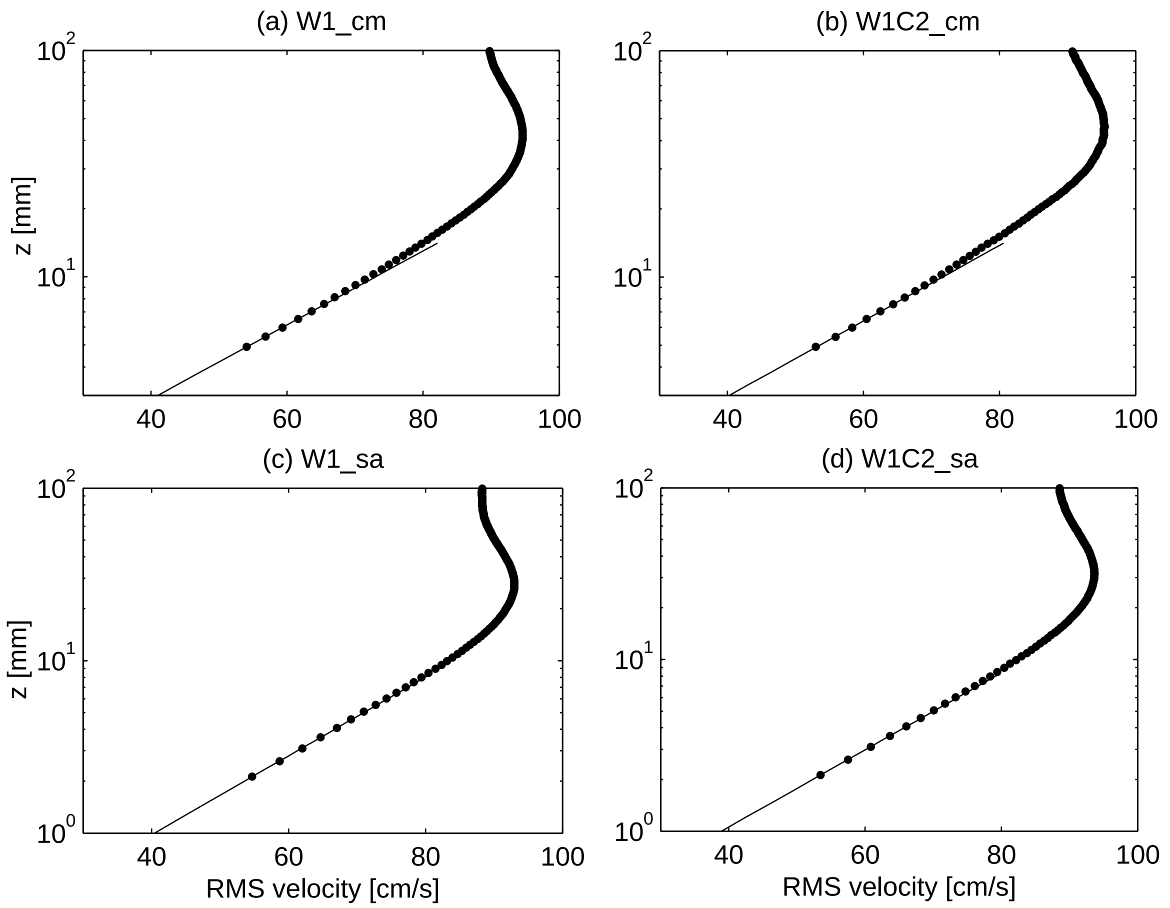

Figure 4. Typical measured RMS velocity profiles and log-profile fittings: (all tests are with the same wave conditions, W1, with target $U_{\infty,rms} = 0.85$ m/s and $T_{ave} = 6.25$ s, the currents in (b) and (d) has an average velocity at about 30cm/s)

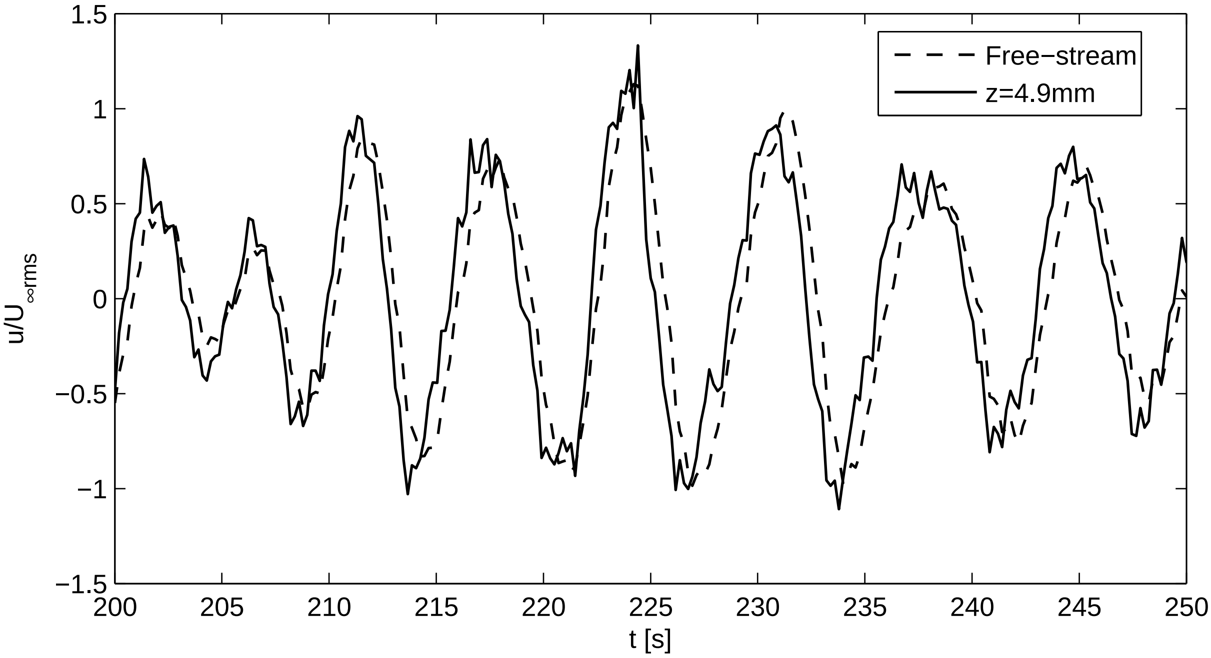

Figure 5. Phase-lead of near-bottom velocity for test W1_cm (solid line: measured velocity at the bottom-most level $z = 4.9$ mm, dashed line: free-stream velocity. The measurements are normalized by their corresponding RMS wave velocities for easy comparison).

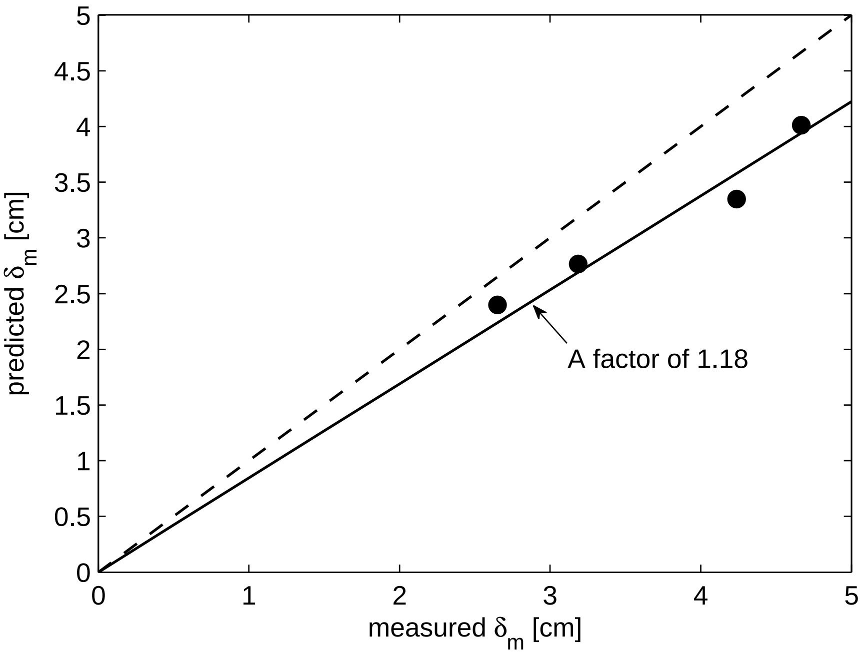

Figure 6. Characteristic boundary layer thickness of irregular wave boundary layers (the dashed line indicates perfect agreement, and solid line is least-square fit to data, of which the slope indicates the overall agreement with measurements.)

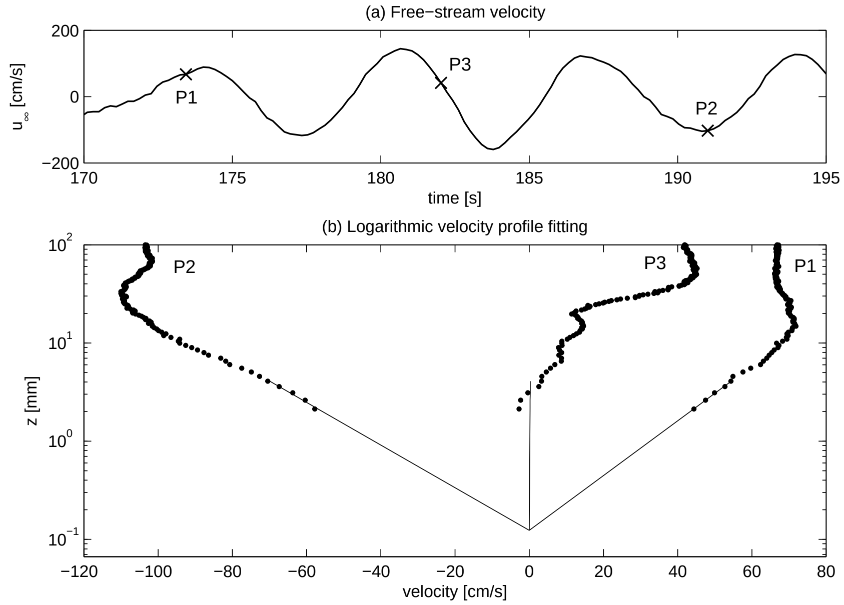

Figure 7. Modified log-profile fitting to the instantaneous velocity profile in the very near-bottom region for test W1_sa ($k_N = 3.7$ mm): (a) free-stream velocity, (b) modified log-profile fittings for three representative instantaneous velocity profiles (solid lines are the fitted logarithmic profiles based on the bottom-most five data points)

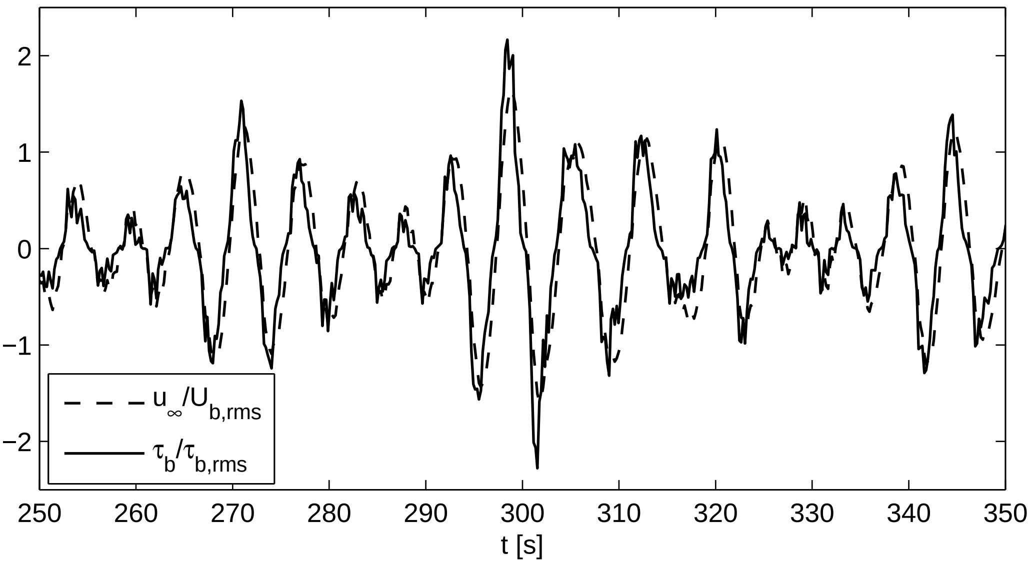

Figure 8. Normalized instantaneous bottom shear stress for test W1_sa

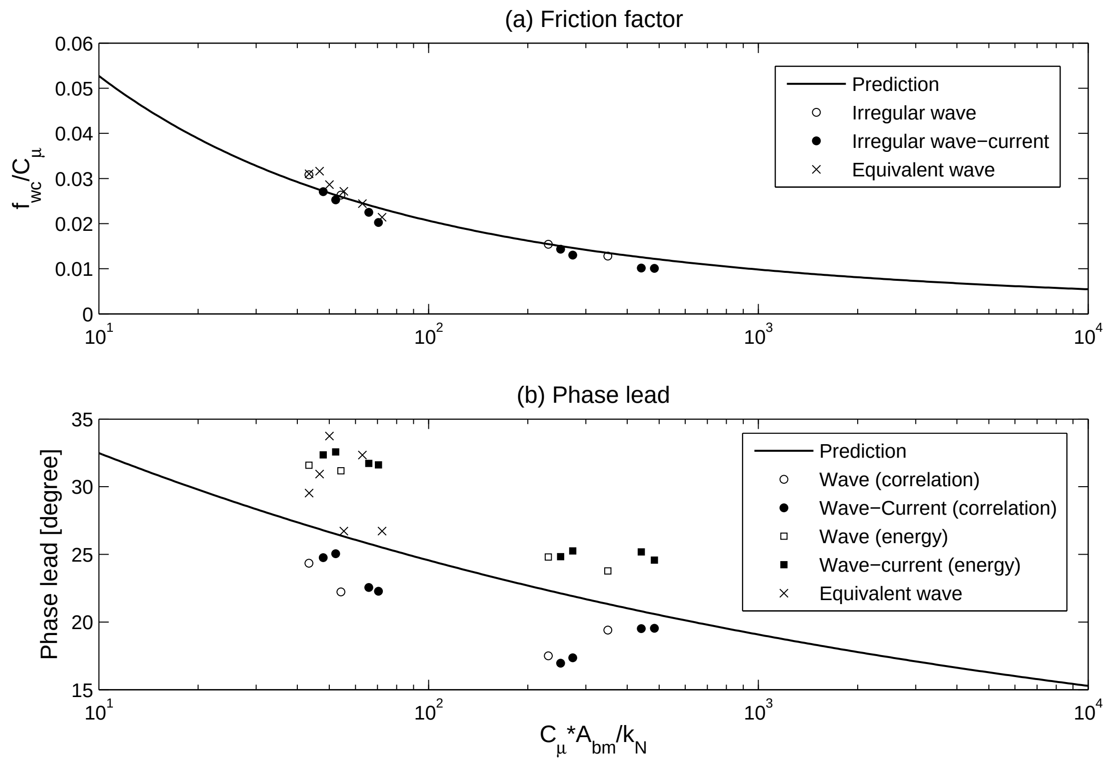

Figure 9. Wave friction factor and phase lead of wave bottom shear stress: (a) wave friction factor, (b) representative phase lead

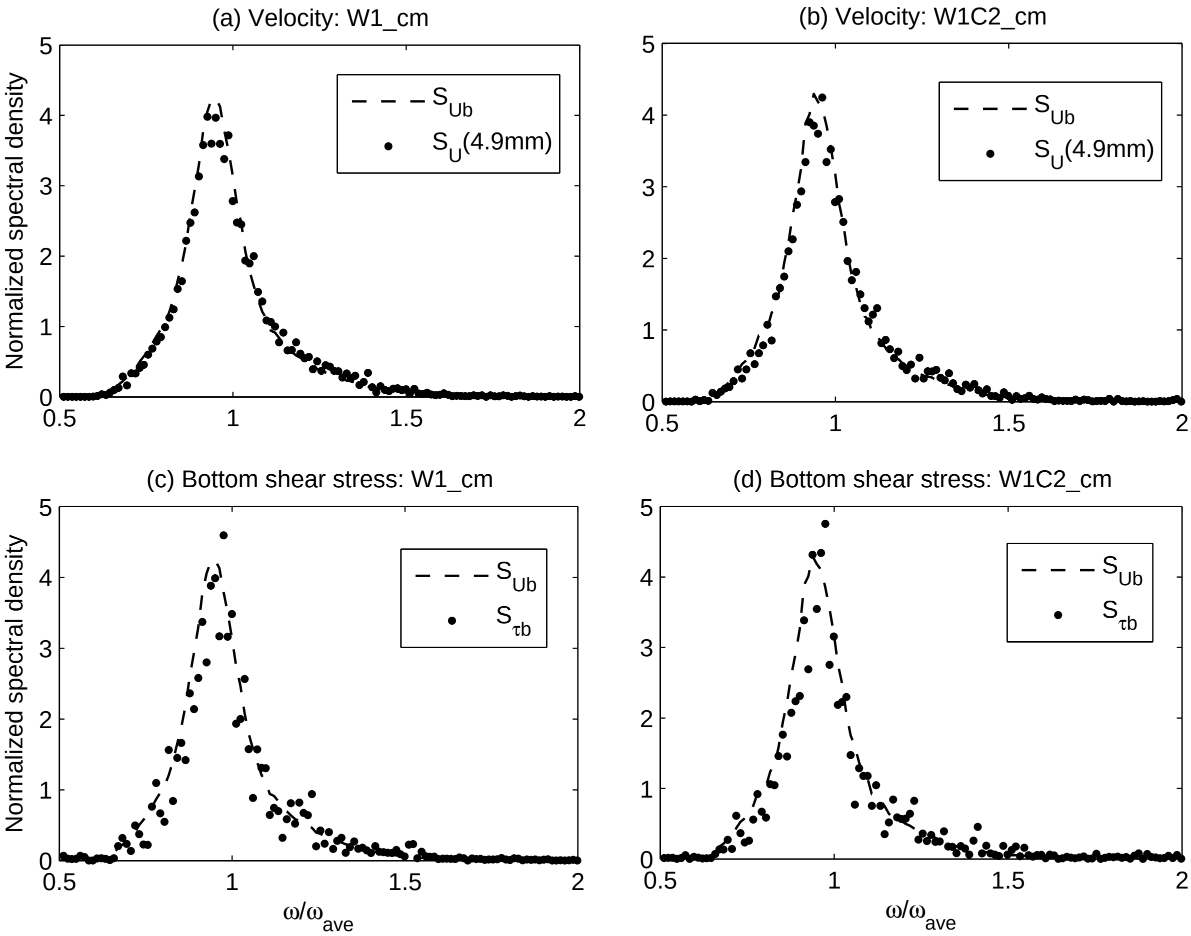

Figure 10. Normalized spectra for near-bottom (z = 4.9 mm) velocities and bottom shear stress: (a) near-bottom velocity of wave-alone test W1_cm, (b) near-bottom velocitiy of wave-current test W1C2_cm, (c) bottom shear stress of wave-alone test W1_cm, (d) bottom shear stress of wave-current test W1C2_cm

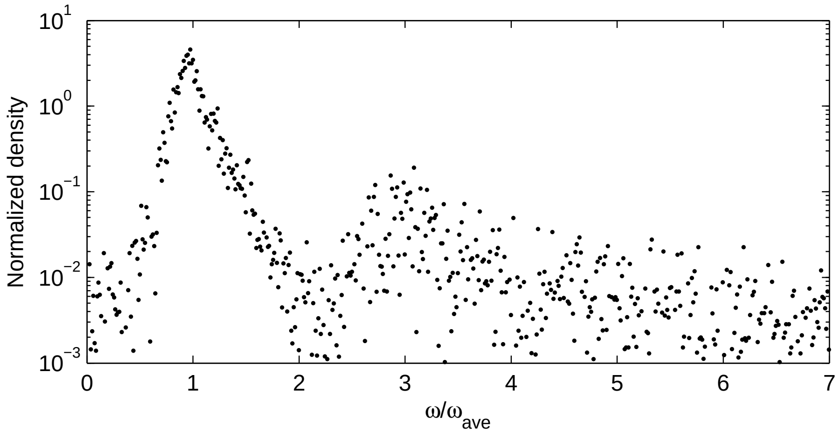

Figure 11. High-frequency part of the spectrum of bottom shear stress for test W1_cm

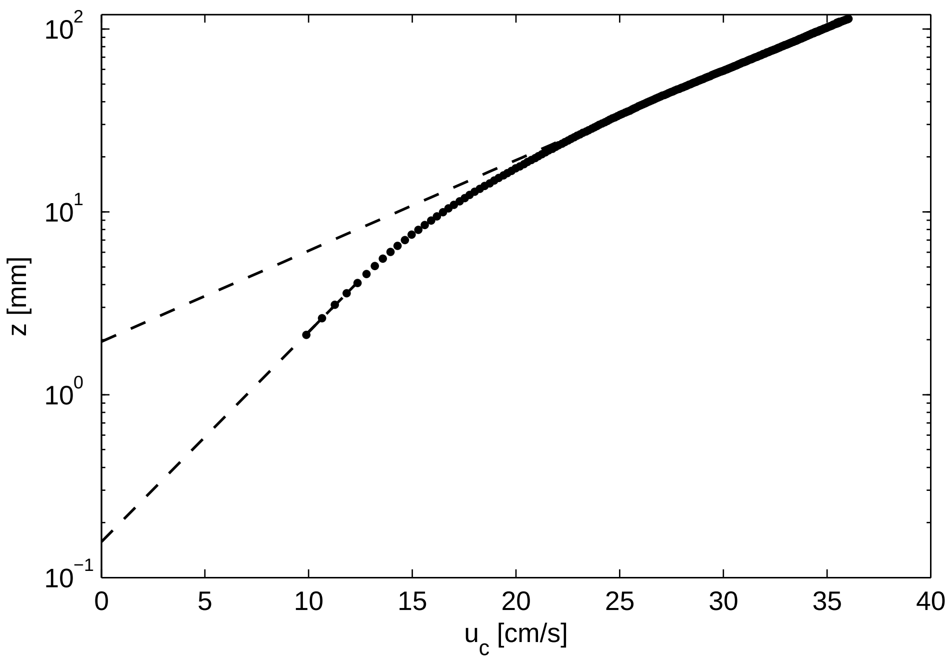

Figure 12. Typical current velocity profile in the presence of irregular waves and fitted logarithmic profiles (test W1C2_sa)

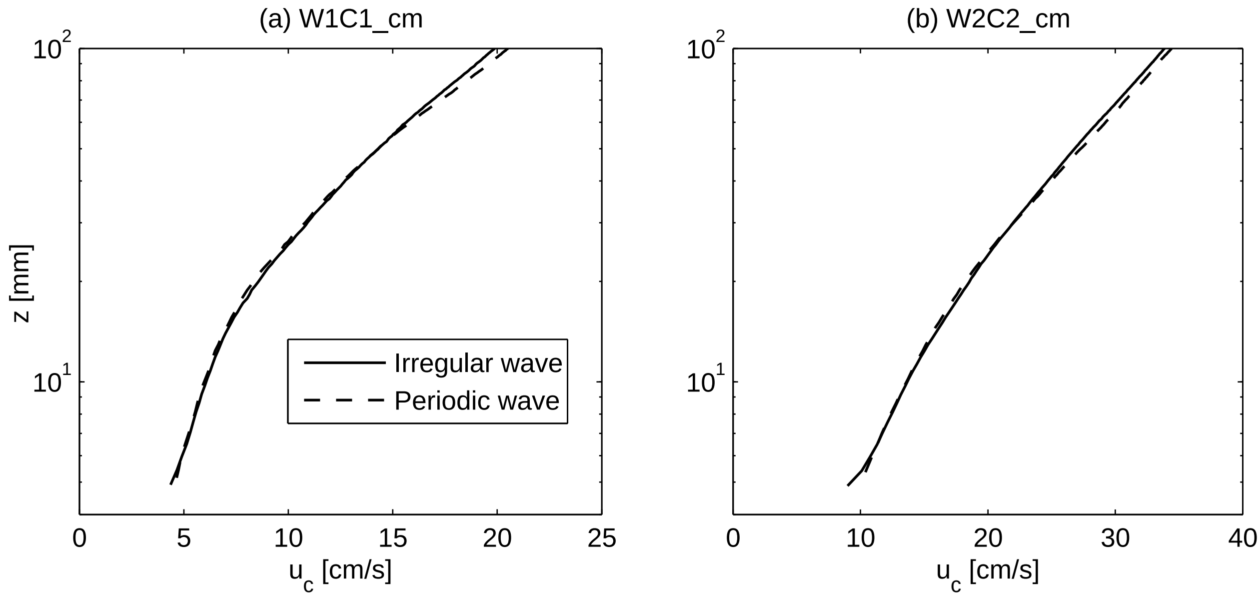

Figure 13. Comparisons of currents in the presence of irregular waves and their equivalent periodic waves: (a) test W1C1_cm, (b) test W2C2_cm (solid lines: current profile with irregular waves, dashed lines: current profile with equivalent periodic waves).

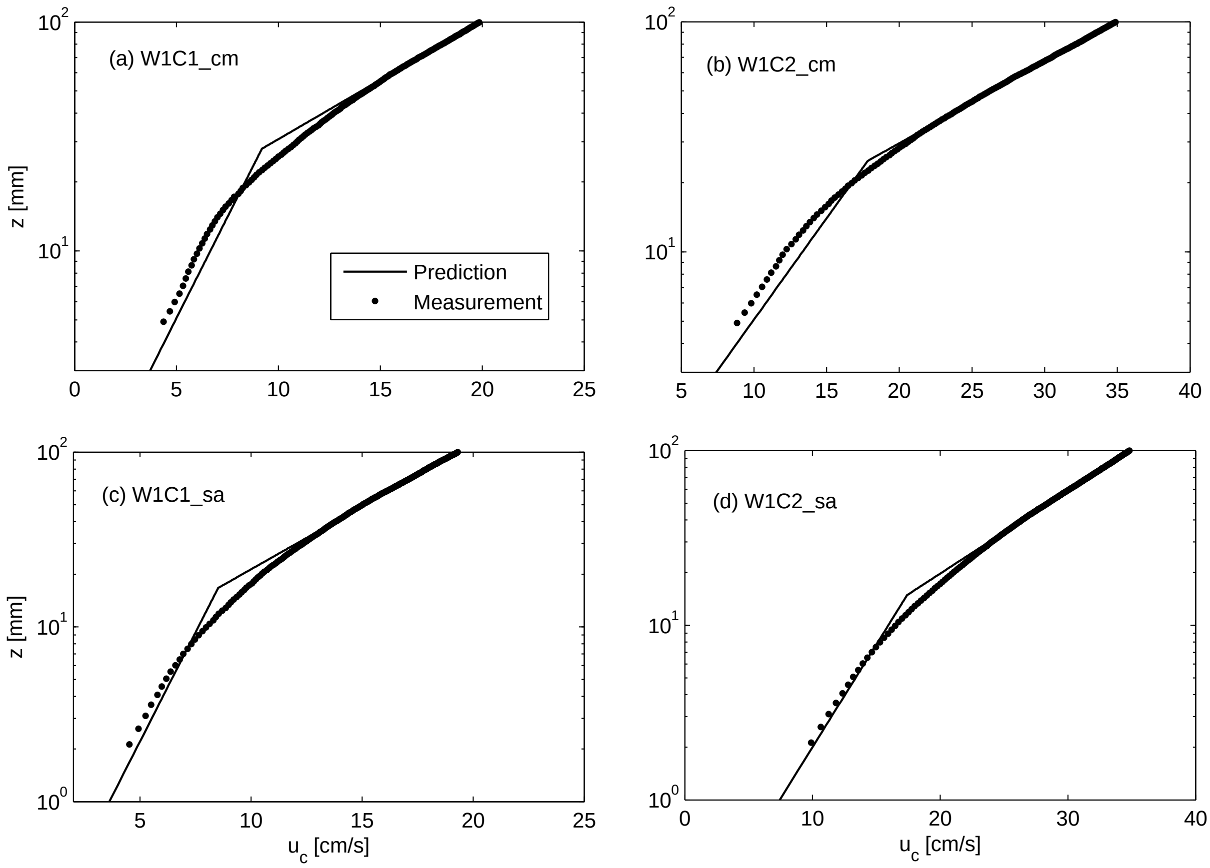

Figure 14. Prediction of current velocity profiles in the presence of irregular waves (dots: measurements, solid lines: predictions).

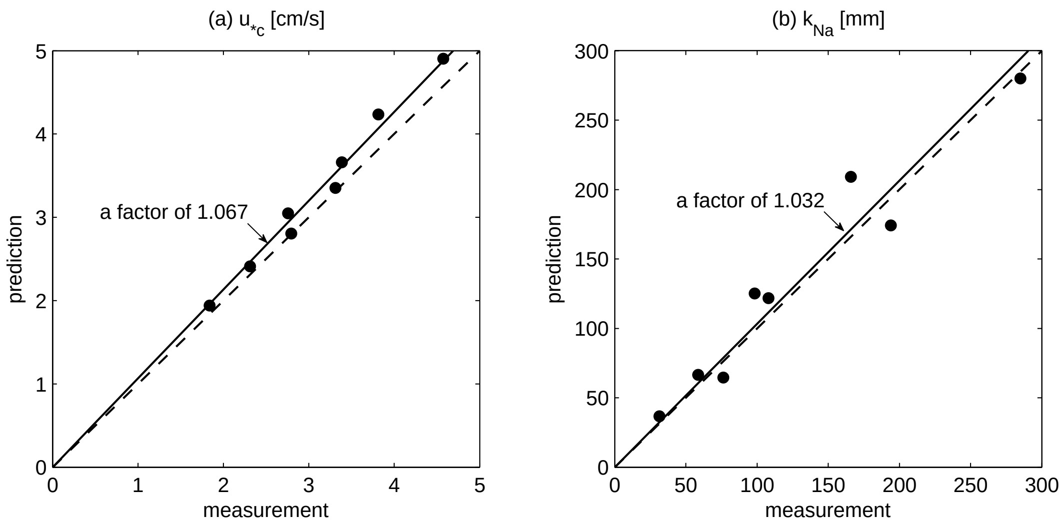

Figure 15. Model validation for current shear velocity and apparent roughness: (a) current shear velocity (b) apparent roughness. The dashed lines indicate perfect agreement, and solid lines are least-square fit to data, of which the slope indicates the overall agreement with measurements.

Table 1. key parameters for the spectra of conceptual surface irregular waves and the associated bottom wave velocities[a]

	Surface wave			Free-stream velocity				
	$h[m]$	H_{rms} [m]	T_p [s]	$U_{\infty,rms}$ [m/s]	T_{ave} [s]	Re	R_u	R_a
W1	12	3.84	6.46	0.85	6.25	$9.0 \cdot 10^5$	0.50	0.50
W2	40	3.98	13.30	0.55	12.50	$7.5 \cdot 10^5$	0.50	0.51

[a] h: water depth, H_{rms}: RMS wave height, T_p: peak period corresponding the peak radian frequency of wave spectrum, $U_{\infty,rms}$: RMS free-stream wave velocity, T_{ave}: average wave period corresponding to the average radian frequency of free-stream velocity spectrum, Re: Reynolds number, R_u and R_a: parameters indicating velocity-skewness and acceleration skewness.

Table 2. Summary of tests [a]

ID	$U_{\infty,rms}$ $[cm/s]$	T_{ave} $[s]$	$u_c, @z_r$ $[cm/s]$	u_{*w} $[cm/s]$	u_{*c} $[cm/s]$	k_b $[mm]$	Re_*
Irregular-wave tests							
W1_sa	88.36	6.07		7.77		3.6	359.2
W2_sa	56.44	11.85		4.52		3.0	209.1
W1C1_sa	88.55	6.06	20.04	7.83	2.31	3.8	377.5
W1C2_sa	88.56	6.04	36.05	7.79	3.39	4.0	392.7
W2C1_sa	56.49	11.66	19.25	4.35	1.84	2.6	218.4
W2C2_sa	56.57	11.57	34.64	4.68	2.76	3.2	251.1
W1_cm	89.43	6.09		11.10		19.2	2774
W2_cm	57.12	11.93		6.55		20.2	1638
W1C1_cm	89.62	6.11	21.21	10.94	3.31	21.9	2858
W1C2_cm	89.86	6.09	37.29	11.06	4.57	19.2	2992
W2C1_cm	57.62	11.97	20.07	6.69	2.80	18.8	1813
W2C2_cm	58.00	11.74	35.78	6.65	3.81	20.3	1915
Equivalent-wave tests							
EW1_cm	89.00	6.06		11.03		19.40	2774
EW2_cm	58.04	11.76		6.75		19.68	1703
EW1C1_cm	88.85	6.06	21.95	11.72	3.50	17.41	3057
EW1C2_cm	89.03	6.06	39.09	11.65	4.67	19.89	3137
EW2C1_cm	57.99	11.76	20.95	6.96	2.77	19.89	1874
EW2C2_cm	58.15	11.76	36.59	6.94	3.97	19.48	1998

[a] $U_{\infty,rms}$: measured RMS free-stream wave velocity, T_{ave}: measured average period of free-stream velocity, u_c: reference current velocity measured at the reference level $z_r = 10$ cm, u_{*c} and u_{*w}: current and wave shear velocities obtained from measured bottom shear stress, k_b: bottom roughness, $Re_* = u_* k_N/\nu$: roughness Reynolds number

Table 3. Log-profile fitting for RMS wave velocity profiles [a]

Test ID	1-R^2	k_b [mm]	$r_{\Delta k}$	u_* [cm/s]	$\Delta u_*/u_*$
W1_cm	$1.7 \cdot 10^{-4}$	19.19	1.05	10.62	2.37%
W1_sa	$1.9 \cdot 10^{-4}$	3.58	1.08	7.60	2.52%
W1C2_cm	$6.2 \cdot 10^{-4}$	19.16	1.11	10.42	4.59%
W1C2_sa	$4.9 \cdot 10^{-5}$	4.02	1.04	7.74	1.01%

[a] 1-R^2: coefficient of determination, u_*: fitted shear velocity, $\pm\Delta u_*/u_*$: relative 95% confidence interval of u_*, k_b: fitted bottom roughness, $r_{\Delta k}$: 95% confidence factor of k_b

Table 4. Log-profile fitting of the current velocity profile and RMS wave velocity profile for Test W1C2_sa [a]

	1-R^2	k_b [mm]	$r_{\Delta k}$	u_* [cm/s]	$\Delta u_*/u_*$
lower profile	$6.3 \cdot 10^{-4}$	4.70	1.15	1.51	4.6%
upper profile	$8.6 \cdot 10^{-4}$	58.59	1.03	3.50	1.0%
RMS wave velocity	$4.9 \cdot 10^{-5}$	4.02	1.04	7.74	1.0%

[a] see the footnote of Table 3 for the definition of variables.